



1 **High-resolution physicochemical dataset of atmospheric**  
2 **aerosols over the Tibetan Plateau and its surroundings**

3 **Jianzhong Xu<sup>1,2\*</sup>, Xinghua Zhang<sup>2,a\*</sup>, Wenhui Zhao<sup>2,3,b</sup>, Lixiang Zhai<sup>2,3,c</sup>, Miao**  
4 **Zhong<sup>2,3</sup>, Jinsen Shi<sup>4</sup>, Junying Sun<sup>5</sup>, Yanmei Liu<sup>2,d</sup>, Conghui Xie<sup>2,e</sup>, Yulong Tan<sup>2,3</sup>,**  
5 **Kemei Li<sup>2,3</sup>, Xinlei Ge<sup>6</sup>, Qi Zhang<sup>7</sup>, Shichang Kang<sup>2,3,8</sup>**

6 <sup>1</sup>School of Oceanography, Shanghai Jiao Tong University, Shanghai 200030, China.

7 <sup>2</sup>State Key Laboratory of Cryospheric Sciences, Northwest Institute of Eco-Environment and  
8 Resources, Chinese Academy of Sciences, Lanzhou 730000, China

9 <sup>3</sup>University of Chinese Academy of Sciences, Beijing 100049, China

10 <sup>4</sup>Key Laboratory for Semi-Arid Climate Change of the Ministry of Education, College of  
11 Atmospheric Sciences, Lanzhou University, Lanzhou 730000, China

12 <sup>5</sup>Key Laboratory of Atmospheric Chemistry of CMA, Chinese Academy of Meteorological  
13 Sciences, Beijing 100081, China

14 <sup>6</sup>Jiangsu Key Laboratory of Atmospheric Environment Monitoring and Pollution Control,  
15 Collaborative Innovation Center of Atmospheric Environment and Equipment Technology,  
16 School of Environmental Science and Engineering, Nanjing University of Information  
17 Science and Technology, Nanjing 210044, China

18 <sup>7</sup>Department of Environmental Toxicology, University of California, Davis, CA 95616, USA

19 <sup>8</sup>CAS Center for Excellence in Tibetan Plateau Earth Sciences, Beijing 100085, China

20 <sup>a</sup>now at: College of Urban and Environmental Sciences, Northwest University, Xi'an 710127,  
21 China.

22 <sup>b</sup>now at: Institute of Geochemistry, Chinese Academy of Sciences, Guangzhou 510640, China.

23 <sup>c</sup>now at: College of Resources and Environmental Sciences, Gansu Agricultural University,  
24 Lanzhou 730000, China.

25 <sup>d</sup>now at: College of Resources and Environment, Aba Teachers University, Wenchuan 623002,  
26 China.

27 <sup>e</sup>now at: State Key Joint Laboratory of Environmental Simulation and Pollution Control,  
28 College of Environmental Sciences and Engineering, Peking University, Beijing 100871, China.

29 *Correspondence to:* Jianzhong Xu ([jzxu78@sjtu.edu.cn](mailto:jzxu78@sjtu.edu.cn); [jzxu@lzb.ac.cn](mailto:jzxu@lzb.ac.cn)) and

30 Xinghua Zhang ([zhangxinghua@lzb.ac.cn](mailto:zhangxinghua@lzb.ac.cn))



31 **Abstract**

32 Atmospheric aerosol in the Tibetan Plateau (TP) and its surroundings has received  
33 widely scientific concern in recent decades owing to its significant impacts on regional  
34 climatic and cryospheric changes, ecological and environmental securities, and  
35 hydrological cycle. However, our understanding on the atmospheric aerosol in this  
36 remote region is highly limited by the scarcely available dataset due to the extremely  
37 harsh natural conditions. This condition has been improved in recent decades by  
38 constructing a few stable field observatories at typical sites on the TP and its  
39 surroundings. A continuous project was carried out since 2015 to investigate the  
40 properties and sources of atmospheric aerosols as well as their regional differences in  
41 the vast TP regions by performing multiple short-term intensive field observations using  
42 a suite of high-resolution online instruments. This paper presents a systematic dataset  
43 of the high-time-resolution (hourly scales) aerosol physicochemical and optical  
44 properties at eight different sites over the TP and its surroundings from the observation  
45 project, including the size-resolved chemical compositions of submicron aerosols,  
46 standard high-resolution mass spectra and sources of organic aerosols, size distributions  
47 of particle number concentrations, particle light scattering and absorption coefficients,  
48 particle light absorptions from different carbonaceous substances of black carbon and  
49 brown carbon, and number concentrations of cloud condensation nuclei. In brief,  
50 atmospheric aerosols in these remote sites were all well-mixed and highly aged due to  
51 their dominated regional transport sources. However, high contributions of  
52 carbonaceous organic aerosols, neutralized bulk submicron aerosols, and relatively  
53 higher light absorption capability were observed in the southern TP region, whereas  
54 secondary inorganic species contributed dominantly to the overall acidic submicron  
55 aerosols in the northern TP region. In addition to the insights into the regional  
56 differences on aerosol sources and properties in the vast TP regions, the datasets are  
57 also useful for the simulation of aerosol radiative forcing and the evaluation of  
58 interactions among different components of the Earth system in numerical models. The  
59 datasets are available from the National Cryosphere Desert Data Center, Chinese  
60 Academy of Sciences (<https://doi.org/10.12072/ncdc.NIEER.db2200.2022>; Xu, 2022).



## 61 **1 Introduction**

62 Tibetan Plateau (TP), with a mean altitude of over 4000 m a.s.l. and a huge surface area  
63 of approximately  $2.5 \times 10^6$  km<sup>2</sup>, is the highest plateau on the Earth. The high-altitude  
64 mountain ranges on the TP and its surroundings are one of the most important  
65 cryospheric regions in the world. Therefore, the TP has been widely known as the “roof  
66 of the world”, the “Third Pole”, or the “Asian Water Tower” (Qiu, 2008; Yao et al.,  
67 2019). The TP and its surroundings have significant impacts in the global and regional  
68 climate systems, hydrological cycles, and cryospheric changes through its huge and  
69 complex topography and heat source (Duan and Wu, 2005; Yao et al., 2012; Chen et al.,  
70 2021). Over the past few decades, one of the most concerns on the TP and its  
71 surroundings has been focusing on the significant climatic warming and rapid  
72 cryospheric changes in this region (Kang et al., 2010), which show a higher warming  
73 rate than the Northern Hemisphere (0.34 vs. 0.29 °C/decade) (You et al., 2021; Zhou  
74 and Zhang, 2021).

75 As the most complex and important component in the atmosphere, atmospheric aerosols  
76 play significant roles in the climatic warming and cryospheric changes in the TP regions  
77 through their crucial direct and indirect effects on solar radiation and the albedos of  
78 snow and ice surfaces (Xu et al., 2009; Kang et al., 2019b). Atmospheric aerosols,  
79 particularly the two important light-absorbing carbonaceous aerosols (CAs) of black  
80 carbon (BC) and brown carbon (BrC), can absorb the solar radiation directly, warm the  
81 atmosphere, and finally lead to a positive forcing on Earth’s energy budget  
82 (Ramanathan et al., 2007; Kopacz et al., 2011). For example, Li et al. (2018) has  
83 simulated significantly higher average albedo reduction (~46%) and instantaneous  
84 radiative forcing (7–64 W m<sup>-2</sup>) caused by BC than mineral dust that deposited on aged  
85 snow in the surface of a TP glacier. In addition, aerosol particles over the TP also exert  
86 significant impacts on ice cloud properties and cloud development through their semi-  
87 direct effects (Liu et al., 2019). Since the direct observation of atmospheric aerosols  
88 over the vast and remote TP regions is remarkably difficult due to the complex  
89 topography and meteorology and harsh environment, the numerical model simulation  
90 based on reanalysis data has become one of the most popular and critical ways over the  
91 past decades. For example, Lau et al. (2006) evaluated the significant impact of  
92 atmospheric aerosols over the TP on the intensification of the Asian summer monsoon  
93 by using the NASA finite-volume general circulation model, of which inputs were



94 driven by the realistic global wind analyses and humidity; Kopacz et al. (2011)  
95 investigated the origin and radiative forcing of BC transported to the TP and Himalayas  
96 by using the GEOS-Chem global chemical transport model based on the global BC  
97 emissions inventory data; Liu et al. (2015) investigated the transport of summer dust  
98 and anthropogenic aerosols over the TP by using a three-dimensional aerosol transport–  
99 radiation model with the inputs from diverse satellite remote sensing products. Although  
100 important findings have been reported from those numerical model simulations, the in-  
101 situ observation of atmospheric aerosols over the TP regions has become more crucial  
102 and urgent due to their key roles in evaluating and improving the model performances  
103 over the remote region. Lacking in-situ observational aerosol parameters for  
104 constraining the model would lead to high uncertainty in the results. In addition, model  
105 simulations in the TP mostly focused on the spatial distribution over a large range, but  
106 rarely on the temporal variations or inherent evolution mechanism with high time  
107 resolution as those from in-situ observations.

108 With great improvements in observational conditions and instruments, numerous in-  
109 situ measurements have been conducted in the TP and its surroundings during the past  
110 few years to characterize the aerosol physical, chemical, and optical properties,  
111 potential sources, transport pathways, and regional distributions. A comprehensive  
112 summary of direct measurements on ambient aerosols in the TP using various  
113 observational methods and instruments has been listed in Table S1 in the supplementary.  
114 Among them, the off-line atmospheric filter sampling was one of the most important  
115 and popular in-situ aerosol collection approach in the TP because it was relatively low-  
116 cost and easy to carry out under the extremely harsh natural conditions and limited  
117 logistical supports. This approach has been successfully conducted to characterize the  
118 compositions, sizes, light absorptions, sources, and variations of ambient aerosols,  
119 especially those different CAs constituents including BC, BrC, organic carbon (OC),  
120 water-soluble OC (WSOC), humic-like substances (HULS), and polycyclic aromatic  
121 hydrocarbons (PAHs), in the remote TP region (Cao et al., 2009; Zhao et al., 2013; Xu  
122 et al., 2014a; Zhang et al., 2014; Cong et al., 2015; Wan et al., 2015; Xu et al., 2015;  
123 Kang et al., 2016; Li et al., 2016b; Xu et al., 2020). In addition, characterizing the  
124 regional distribution of atmospheric aerosols over a large area of the TP was another  
125 important advantage of the off-line filter sampling through their simultaneous  
126 observations at multiple sites due to the relatively easy instrumental operations (Li et



127 al., 2016a; Chen et al., 2019; Kang et al., 2022). However, studies on the atmospheric  
128 aerosols over the remote TP regions through these off-line filter samplings are still  
129 scarce and far meeting the demand at present. These observational data was generally  
130 scattered and unsystematic with relatively low time resolution, few aerosol property  
131 parameters, and less data points because most of them were carried out at certain site  
132 using single instruments with time resolutions from days to weeks during a short-term  
133 period. The low time resolution measurement would limit the accurate understanding  
134 of temporal evolution processes and mechanisms of aerosol properties during a fast and  
135 short-term event. Meantime, these observational data from different research groups  
136 was also difficult to compare and integrate because most of them had different research  
137 concerns, measurement parameters, sampling flows, laboratory filter treatment  
138 procedures, data analysis methods, etc. Besides, although the off-line sampling is  
139 relatively easy to carry out, there are still large TP regions where similar observations  
140 have not yet been conducted or only conducted in a short-term period. Up to now,  
141 comprehensive research focusing on multiple aerosol physicochemical and optical  
142 properties through the real-time online consecutive measurements (high temporal  
143 resolutions from minute to hour scales) at multiple sites are still rare in the TP.

144 Studies on atmospheric aerosols have achieved great progress during the last decade in  
145 China. The Aerodyne high-resolution time-of-flight aerosol mass spectrometer (HR-  
146 ToF-AMS) was one of the most popular online instrument that successfully  
147 implemented in numerous aerosol chemistry observations to characterize the real-time  
148 size-resolved chemical compositions and sources of submicron aerosols (Li et al., 2017;  
149 Zhou et al., 2020). However, the utilization of HR-ToF-AMS on the TP was still very  
150 scarce due to the high instrumental requirements but extremely harsh observation  
151 conditions. Since 2015, a continuous and systematic observation project, aiming to  
152 investigate the regional differences on aerosol sources and properties in the different  
153 TP regions, has been launched by our research team by performing HR-ToF-AMS  
154 measurement and other high-resolution real-time online instruments at different sites  
155 during almost every year. Indeed, our dataset was the first and only set of dataset  
156 focusing on abundant aerosol parameters (including the physical, chemical, and optical  
157 properties and diverse sources) at multiple different types of site (e.g., the urban, remote,  
158 high-altitude mountain, grassland, and subtropical forest sites that basically represented  
159 the different TP regions) based on the real-time high-time-resolution online



160 observations in the TP and its surroundings. These datasets provide not only  
161 comprehensive data for the understanding of regional differences in aerosol sources and  
162 properties in different TP regions, but also potential basic inputs for the simulation of  
163 aerosol radiative forcing and the assessments of interactions among different  
164 components of the Earth system in future models. The contents of this paper are  
165 organized as: Sects. 2 and 3 describe the observation sites, instrumental deployments,  
166 and data processing methods, Sect. 4 introduces the high-time-resolution data of aerosol  
167 physical, chemical, and optical properties as well as sources, while the limitations and  
168 uniqueness of our dataset are discussed in Sect. 5.

## 169 **2 Observation site descriptions**

170 Continuous observations of atmospheric aerosol chemistry were conducted at eight  
171 sites in the different regions of TP and its surroundings from 2015 to 2022. The sites  
172 include seven remote sites (QOMS, Motuo, NamCo, Ngari, Waliguan, LHG, and  
173 Bayanbulak) and one urban site (Lhasa) which is used for comparison. Figure 1  
174 illustrates the geographical locations of these sites and the picture of each observation.  
175 Table 1 provides detailed information of each site as well as the sampling period and  
176 available instruments during each field campaign. The following text gives a brief  
177 description of each site from the south to north of the TP.

### 178 **2.1 QOMS**

179 The Qomolangma Station for Atmospheric and Environmental Observation and  
180 Research, Chinese Academy of Sciences (QOMS for short in this study and similarly  
181 hereinafter for other sites; 86.56°E, 28.21°N; 4276 m a.s.l.) is situated in the basin of  
182 Rongbuk valley in the northern slope of Mt. Everest. The climate in the northern slope  
183 of Mt. Everest has obvious seasonal variation under the influence of Indian monsoon  
184 system (Bonasoni et al., 2010; Cong et al., 2015). During the pre-monsoon season  
185 (generally March–May), the dominated westerlies play important roles in the long-  
186 range transport of atmospheric pollutants from those polluted regions in South Asia,  
187 which makes QOMS an ideal high-altitude observatory at the south edge of the TP for  
188 studying the transboundary transport of atmospheric pollutants from South Asia to the  
189 inner TP. During the monsoon season in summer (June–August), the southerly winds  
190 prevail and bring warm and wet airflow from the Indian Ocean to this region with  
191 increasing humidity and precipitation.



192 **2.2 Motuo**

193 Motuo county is in the lower reaches of the Yarlung Tsangpo River and the southern  
194 slope of the eastern Himalayas and Gangrigab Mountains in the southeast edge of the  
195 TP. The county sits at a halfway up a mountain and has a subtropical humid climate  
196 with relatively high temperature and abundant rainfall. Due to the minor population  
197 (~15,000), Motuo county is also a relatively pristine region in the TP. The sampling site  
198 in Motuo (29.30°N, 95.32°E; 1305 m a.s.l.) was at the summit of a hill that towards to  
199 the Yarlung Tsangpo Grand Canyon, which makes it a very ideal site in the southeast  
200 edge of the TP to directly monitor the transboundary transport of atmospheric pollutants  
201 and moisture from Southeast Asia and Indian Ocean to the TP.

202 **2.3 NamCo**

203 The Nam Co Station for Multisphere Observation and Research, Chinese Academy of  
204 Sciences (NamCo; 90.95°E, 30.77°N; 4730 m a.s.l.) is a high-altitude observatory at the  
205 south-central part of the TP. This station is situated at the southeast shore of Nam Co  
206 Lake. The surrounding of this station is a pristine region in the TP and isolated from  
207 major populated areas. The region is generally affected by the typical semi-arid plateau  
208 monsoon climate with more precipitation during the summer monsoon season. The  
209 NamCo is the most important site in inland of the TP and dominated by air mass from  
210 south and west.

211 **2.4 Ngari**

212 The Ngari Station for Desert Environment Observation and Research, Chinese  
213 Academy of Science (Ngari; 79.70°E, 33.39°N; 4270 m a.s.l.) locates in the Rutog  
214 County, Ngari Prefecture, Tibet Autonomous Region, China. This region is the  
215 southwestern edge of the TP and belongs to semi-arid areas with barren land surface  
216 and strong solar radiation. As the major member of the “high-cold region observation  
217 and research network for land surface processes & environment of China”, Ngari station  
218 is one of the most important filed stations for monitoring the changes in climate,  
219 hydrology, atmosphere, and ecological environment in the western region of the TP and  
220 further revealing the interaction between the Indian monsoon and the westerly belt.

221 **2.5 Waliguan**

222 The Waliguan Baseline Observatory (Waliguan; 100.9°E, 36.28°N; 3816 m a.s.l.) is one  
223 of the twenty-nine baseline stations of Global Atmosphere Watch (GAW) of the World



224 Meteorological Organization (WMO). The observatory is situated at the top of the Mt.  
225 Waliguan (mountain height of ~600 m), which is also a relatively pristine region with  
226 little influence from human activities. The Waliguan is an important observatory in the  
227 northeast edge of the TP and dominated by air mass from northeast during the summer  
228 season, which makes it an ideal site to study the influence of air pollutants from the  
229 industrial areas in the northwestern China to the TP.

## 230 **2.6 LHG**

231 The Qilian Observation and Research Station of Cryosphere and Ecologic Environment,  
232 Chinese Academy of Sciences (LHG; 39.50°N, 96.51°E; 4180 m a.s.l.) locates near the  
233 terminus (~1 km) of the Laohugou Glacier No.12, which is one the largest mountain  
234 glacier in the northern slope of the western Qilian Mountains. LHG is another  
235 representative station in the northeastern TP and significantly isolated from the human  
236 living areas. The climate in this region is a typically arid and continental climate and  
237 dominated by the East-Asian monsoon in the summer and Westerlies in the winter.  
238 Strongly mountain-valley breeze is formed during summer which can bring air mass  
239 from lower altitude zones to mountain regions. Therefore, it is also well suited for  
240 sampling the background air mass and studying the transport mechanisms and potential  
241 impacts of air pollutants from its surrounding regions.

## 242 **2.7 Bayanbulak**

243 The Bayanbulak National Basic Meteorological Station (Bayanbulak; 84.35° N, 42.83°  
244 E; 2454 m a.s.l.) locates in the Bayanbulak grassland at the northwest of Hejing county,  
245 Xinjiang Uygur Autonomous Region, China. The Bayanbulak is situated in an  
246 intermontane basin in the central Tianshan Mountains and surrounded by numerous  
247 snow mountains with altitudes more than 3000 m. The climate in Bayanbulak grassland  
248 belongs to the typical temperate continental mountain climate with an annual average  
249 precipitation of about 200–300 mm. The Bayanbulak town has limited human activities  
250 and traffic transportation.

## 251 **2.8 Lhasa**

252 Lhasa (29.65°N, 91.03°E; 3650 m a.s.l.) is the capital city of the Tibet Autonomous  
253 Region, China that located in the south-central part of the TP. The city lies in a flat river  
254 valley with the surrounding mountains reaching 5500 m and the Lhasa River passing  
255 through the city from west to east. The observation site in Lhasa is in the Binhe Park





256 near the Lhasa River. The Norbulingka scenic area, one of the main activity centers for  
257 local Tibetans to celebrate their religious festivals (e.g., the Sho Dun festival), is located  
258 ~1 km to the northwest of the sampling site, while the Potala Palace, the center of  
259 Tibetan Buddhism, is ~1.8 km to the northeast. Since the unique energy structure and  
260 different residential habit in Lhasa comparing with those remote sites, a comparative  
261 observation is conducted in this urban site for studying the primary aerosol properties  
262 and sources from various residential combustion activities.

### 263 **3 Online sampling, instrumental setup, and data processing**

#### 264 **3.1 Online real-time aerosol sampling over the TP**

265 The online-based observations of atmospheric aerosols were carried out at each site  
266 using a suit of real-time high-resolution instruments, usually including a HR-ToF-AMS  
267 (Aerodyne Research Inc., Billerica, MA, USA) for acquiring the chemical compositions  
268 (organic aerosol (OA), nitrate, sulfate, ammonium, and chloride) of non-refractory  
269 submicron aerosol (PM<sub>1</sub>), a scanning mobility particle sizer (SMPS, model 3936, TSI  
270 Inc., Shoreview, MN, USA) for acquiring the size distribution of number concentration  
271 of submicron particles, a photoacoustic extinctions (PAX, DMT Inc., Boulder, CO,  
272 USA) for acquiring the particle light absorption, scattering, and extinction coefficients  
273 ( $B_{abs}$ ,  $B_{scat}$ , and  $B_{ext}$ ) and single scattering albedo (SSA) at 405 nm as well as the mass  
274 concentration of BC, an Aethalometer (model AE33/AE31, Magee Scientific Corp.,  
275 Berkeley, CA, USA) for acquiring the  $B_{abs}$  at seven fixed wavelengths (370–950 nm),  
276 and a cloud condensation nuclei (CCN) counter (model CCN-100, DMT Inc., Boulder,  
277 CO, USA) for acquiring the CCN number concentration at different supersaturation ( $SS$ )  
278 of water vapor. The specific instrumental deployment and sampling period during each  
279 observation campaign is summarized in Table 1.

280 The HR-ToF-AMS, serving as the primary instrument for observing atmospheric  
281 aerosol chemistry, was deployed throughout all field campaigns. The SMPS was  
282 utilized at QOMS, Motuo, LHG, and Lhasa, while the PAX was employed at QOMS,  
283 Motuo, Ngari, Waliguan, and Lhasa. Additionally, the Aethalometer was utilized at  
284 QOMS, NamCo, and Waliguan, and the CCN-100 at Motuo, Waliguan, and LHG. Field  
285 observations in the southern, western, or central TP regions were predominantly  
286 conducted during the pre-monsoon periods. For instance, observations took place from  
287 12 April to 12 May at QOMS, 26 March to 22 May at Motuo, 31 May to 1 July at  
288 NamCo, and 1 Jun to 5 July at Ngari, which were to investigate the transboundary



289 transport of atmospheric pollutants from polluted regions in South Asia to the inland  
290 areas of the TP, considering the influences of Westerlies and the Indian monsoon. On  
291 the other hand, measurements in the remote regions of the northern TP and its  
292 surroundings were carried out during the summer. Specifically, observations occurred  
293 from 1 to 31 July at Waliguan, 4 to 29 August at LHG, and 29 August to 26 September  
294 at Bayanbulak. These measurements were undertaken to monitor the aerosols  
295 transported from surrounding polluted regions, considering the influences of Westerlies  
296 or the intensified East Asian monsoon. The observation in Lhasa was conducted  
297 between 31 August and 26 September focusing on the strongest atmospheric oxidation  
298 capability during the summer season.

### 299 **3.2 Instrumental setup**

300 Despite variations in the instruments used during different observation campaigns, the  
301 sampling settings remain generally consistent. Figure 1b illustrates the fundamental  
302 sampling setup employed for each campaign. All instruments are typically housed  
303 within an air-conditioned trailer or room. The inlets are induced to the instruments from  
304 the roof with a fine particle cyclone (model URG-2000-30EH, URG Corp., Chapel Hill,  
305 NC, USA) in the front of the inlet to eliminate particles with an aerodynamic diameter  
306 ( $D_{va}$ ) exceeding 2.5  $\mu\text{m}$ . Subsequently, the fine particles are directed into a Nafion dryer  
307 via 1/2-inch stainless steel tubes to remove moisture from the airflows. Lastly, the  
308 particles are sampled into a series of online instruments for real-time measurements.  
309 For a more comprehensive understanding of the instrumental setups, please refer to our  
310 previous publications (Xu et al., 2018; Zhang et al., 2018; Zhang et al., 2019; Zhao et  
311 al., 2022).

### 312 **3.3 Instrumental operation and data processing**

313 The measurement principles, operation procedures, calibration methods, and data  
314 analysis for these instruments are extensively described in detail in Text S1–4 in the  
315 supplementary materials of this study. Only a few essential descriptions and important  
316 settings are emphasized here as follows: (1) The HR-ToF-AMS instruments were  
317 operated at the V-mode during almost all the eight field campaigns, considering the  
318 relatively low aerosol mass levels and signal-to-noise ratios over the TP regions. (2)  
319 Due to chopper malfunction in the HR-ToF-AMS, particle size observations were not  
320 conducted during the NamCo and LHG campaigns. (3) Different relative ionization



321 efficiency values were used for ammonium and sulfate according to the ionization  
322 efficiency calibrations of HR-ToF-AMS in different campaigns, while default values  
323 were used to rest species. (4) Different size parameters were achieved according to the  
324 particle sizing calibrations in different campaigns, which ultimately resulted in the  
325 distinct size ranges of non-refractory PM<sub>1</sub>. (5) Elemental ratios of OA, i.e., oxygen-to-  
326 carbon (O/C), hydrogen-to-carbon (H/C), organic matter-to-organic carbon (OM/OC),  
327 and nitrogen-to-carbon (N/C), were determined using the improved method  
328 (Canagaratna et al., 2015). (6) Default collection efficiency (CE) values of 0.5 were  
329 employed to the HR-ToF-AMS measurements during the QOMS, NamCo, Ngari,  
330 Waliguan, and Lhasa campaigns in consideration of their overall neutralized bulk  
331 submicron aerosols, whereas the composition-dependent CE (Middlebrook et al., 2012)  
332 values are adopted at Motuo, LHG, and Bayanbulak, where bulk submicron aerosols  
333 were slightly acidic. (7) Source apportionments of OA during all observations were  
334 performed by the positive matrix factorization (PMF) analysis method. (8) Only the  
335 chemical compositions of non-refractory PM<sub>1</sub> are reported during the Bayanbulak  
336 campaign due to the absence of BC observations. (9) The sample and sheath flow rates  
337 of SMPS were set at 0.3 and 3.0 L min<sup>-1</sup>, respectively, at both QOMS and Lhasa,  
338 measuring particles between 14.6 and 661.2 nm in mobility diameter ( $D_m$ ), whereas 0.5  
339 and 5.0 L min<sup>-1</sup> at LHG and Motuo sites with a particle size range of 10.9–495.8 nm in  
340  $D_m$ . (10) Aethalometer measurement were corrected for both the filter-based loading  
341 effect and multiple scattering effect. A traditional absorption Ångström exponents  
342 (AAE) method (Zhang et al., 2021) was adopted to quantitatively apportion the total  
343  $B_{abs}$  into two parts from BC and BrC ( $B_{abs,BC}$  and  $B_{abs,BrC}$ ). (11) During the Motuo,  
344 Waliguan, and LHG campaigns, the number concentrations of CCN were conducted  
345 consecutively at five different  $SS$  values of 0.2%, 0.4%, 0.6%, 0.8%, and 1.0% every 5  
346 minutes.

## 347 **4 Aerosol properties, sources, and radiative forcing over the TP**

### 348 **4.1 Mass loading and chemical composition of submicron aerosols**

349 Figure S1 provides an overview of the high-time-resolution temporal variations of PM<sub>1</sub>  
350 chemical species (OA, nitrate, sulfate, ammonium, chloride, and BC) during the eight  
351 observations in the TP and its surroundings. Generally, the mass concentrations of PM<sub>1</sub>  
352 and its chemical species varied dynamically, with alternating periods of high and low  
353 mass loading throughout the sampling period of each campaign. Despite differences in



354 sampling years (2015–2022), seasons (March–September), and altitudes (1350–4730  
355 m a.s.l.) at these sites, the significantly distinct PM<sub>1</sub> mass and chemical compositions  
356 can effectively reflect the regional difference in aerosol mass levels, properties, and  
357 sources at different regions. On average, the mass concentration of total PM<sub>1</sub> across the  
358 eight campaigns ranged from 1.9 to 9.1  $\mu\text{g m}^{-3}$  (Fig. 2 and Table 2). The highest PM<sub>1</sub>  
359 mass was observed at Waliguan due to the rapid transport of anthropogenic aerosols  
360 and gaseous pollutants from urban areas in northwestern China. Conversely, the lowest  
361 values were measured at NamCo and Bayanbulak, attributed to their background and  
362 pristine environmental conditions. The average PM<sub>1</sub> mass level in the TP and its  
363 surroundings was comparable to values observed at other high-altitude, coastal, forest,  
364 and remote background sites worldwide (0.46–15.1  $\mu\text{g m}^{-3}$ ; Table 3), but significantly  
365 lower than those observed at densely urban (34.4–71.5  $\mu\text{g m}^{-3}$ ) and suburban  
366 (21.4–44.9  $\mu\text{g m}^{-3}$ ) sites in other regions of China (Li et al., 2017), suggesting the  
367 predominantly clean nature of atmosphere condition in the remote high-altitude regions  
368 of the TP.

369 The chemical compositions of PM<sub>1</sub> also exhibited significant regional difference (Fig.  
370 2), indicating distinct aerosol sources across different TP regions. OA and BC together  
371 contributed as high as 64.9–85.7% of the total PM<sub>1</sub> mass at the five sites of QOMS,  
372 Motuo, NamCo, Ngari, and Lhasa that are located in the southern, western, or central  
373 TP (Table 2). These high contributions were mainly attributed to the frequent transport  
374 of biomass-burning-related emissions from polluted regions in South and Southeast  
375 Asia to the remote sites of TP during the pre-monsoon season (Bonasoni et al., 2010;  
376 Cong et al., 2015; Zhang et al., 2018) as well as the intense local biomass burning  
377 emissions from religious activities in the urban area of Lhasa (Cui et al., 2018; Zhao et  
378 al., 2022). In contrary, the three inorganic species (sulfate, nitrate, and ammonium;  
379 referred to as SNA) accounted for more than 60% of the total PM<sub>1</sub> at three northern  
380 sites (Waliguan, LHG, and Bayanbulak). Among these, sulfate had the most dominant  
381 contributions of SNA (38.1–46.0%), consistent with the results observed at another  
382 high-altitude site in the northeastern TP (Menyuan; 28%) and other rural and remote  
383 sites (19–64%) in East Asia, indicating the regional transported sources (Du et al., 2015).  
384 The high contributions of SNA, particularly the sulfate, in the northern TP and its  
385 surroundings were mainly related to the regional transport of anthropogenic aerosols  
386 and gaseous precursor emissions from surrounding urban areas as well as important in-



387 cloud aqueous reactions during the transportation to the mountains (Zhang et al., 2019).

#### 388 **4.2 Bulk acidity, size distribution, and diurnal variation of submicron aerosols**

389 Particle phase acidity is an important parameter affecting the physicochemical  
390 properties of aerosol, with significant impacts on hygroscopic growth, toxicity, and  
391 heterogeneous reactions of aerosol particles. The bulk acidity of submicron aerosols  
392 was evaluated at each site following the method in Zhang et al. (2007b) and  
393 Schueneman et al. (2021) based on AMS measurements. A detailed description of this  
394 method can be found in our previous publications (Zhang et al., 2018; Zhang et al.,  
395 2019) or in Text S5 in the supplementary materials of this study. It is interesting to find  
396 that the bulk acidity of submicron aerosols exhibited distinct regional difference  
397 between the southern and northern TP (Fig. 3), primarily attributed to variations in  
398 aerosol sources and compositions. Linear regression slopes were fitted to be 1.2, 1.11,  
399 0.98, and 1.18 at the four sites of QOMS, NamCo, Ngari, and Lhasa that locates in the  
400 southern, western, or central TP, indicating the submicron aerosol particles at these sites  
401 were generally neutralized, and in some cases, showed an excess of ammonium. The  
402 finding is consistent with previous observations of high ammonia availability resulted  
403 from agriculture emissions in the South Asia (Van Damme et al., 2015). In addition, as  
404 reported in our previous publications, atmospheric aerosols at QOMS and NamCo were  
405 significantly influenced by the transport of biomass-burning-related emissions from  
406 South and Southeast Asia during the pre-monsoon season (Xu et al., 2018; Zhang et al.,  
407 2018), while various residential biomass fuels were burned intensely during those  
408 frequent religious festivals in urban areas of Lhasa (Zhao et al., 2022). In contrast, the  
409 submicron particles were overall acidic with regression slopes ranging from 0.73 to  
410 0.86 at the remaining four sites, especially in the two northern sites (LHG and  
411 Bayanbulak), where sulfate significantly contributed to the total PM<sub>1</sub> (46.0% and  
412 41.6%). Similar observations of acidic submicron aerosol particles have also been  
413 observed at Menyuan and LHG in the northern TP in previous studies (Du et al., 2015;  
414 Xu et al., 2015), mainly related to the transport of the enriched SNA species or their  
415 gaseous precursors from the industrial areas in northwestern China to the remote  
416 regions in the northern TP.

417 The size distributions of non-refractory PM<sub>1</sub> chemical species, obtained from HR-ToF-  
418 AMS measurement, provide valuable insights into aerosol sources, oxidation degrees,  
419 mixing states, formation, transformation, and growth mechanisms as well as their



420 impacts on CCN activity. Typically, the size distributions peaked at accumulation mode  
421 ( $\sim 400\text{--}600$  nm in  $D_{va}$ ) for those SNA species and oxidized OA components as a result  
422 of their secondary formation. In contrast, fresh organics from primary emission sources  
423 had smaller sizes (Zhang et al., 2005b; Aiken et al., 2009). In this study, both organics  
424 and the sum of three SNA species were selected to illustrate the regional difference in  
425 size distributions across the different TP regions. As shown in Figs. 4a and S2 and Table  
426 2, the peak diameters in the size distribution of OA and SNA varied significantly,  
427 ranging from 584.4 and 634.5 nm at Ngari to a smaller size of 228.1 and 250.0 nm at  
428 Lhasa, respectively. This suggests distinctly different sources and aging processes of  
429 atmospheric aerosols in different TP regions, particularly between those high-altitude  
430 remote sites and urban sites. For example, bulk  $PM_{10}$  was reported to be internally well-  
431 mixed and aged at QOMS due to long-range transport aerosol sources of biomass-  
432 burning-related emissions from South Asia (Zhang et al., 2018), whereas local primary  
433 sources including cooking, traffic exhausts, and biomass burning together contributed  
434 more than 60% of the total OA at the urban site in Lhasa (Zhao et al., 2022). The crucial  
435 influence of aerosol sources on size distributions is further supported in Fig. 4a by the  
436 quantitative relationship between the mode size and O/C ratios of OA ( $R^2 = 0.74$ ).

437 The diurnal variations of  $PM_{10}$  chemical compositions are typically influenced by  
438 multiple factors, including the meteorological conditions (such as planetary boundary  
439 layer (PBL) height, wind direction and speed, temperature, relative humidity), different  
440 primary emission sources (such as intense vehicle exhausts during traffic rush hours,  
441 cooking emissions, and coal combustion emissions from heating activities), and distinct  
442 formation mechanisms (such as daytime photochemical oxidation processes, nighttime  
443 heterogeneous reactions, and gas-particle partitioning of secondary species). Therefore,  
444 a comprehensive understanding of the diurnal variation characteristics of different  
445 aerosol chemical compositions is not only beneficial for investigating their dynamic  
446 evolution processes but also helpful in understanding the key factors (source,  
447 meteorology, or secondary formation) that drive the variations of different chemical  
448 species. Clearly, different diurnal variation patterns of the total  $PM_{10}$  mass  
449 concentrations were observed during the different field campaigns (Fig. 4b). The  
450 diurnal variations at those remote sites (such as QOMS, LHG, NamCo, and Waliguan)  
451 located either in the valley or at the top of the mountains were mostly controlled by the  
452 circulation of mountain-valley wind and the variation of PBL height during the day.



453 QOMS exhibited a distinct diurnal pattern with continuously decreasing concentrations  
454 during the daytime, but relatively higher concentrations at night. The minimum mass  
455 occurred at around ~15:00 in this valley site, mainly due to the strong down-slope  
456 glacier winds with high wind speed and enhanced PBL height in the afternoon (Zhang  
457 et al., 2018). Conversely, lower PM<sub>1</sub> mass concentration from night to early morning  
458 and continuously increasing concentrations during the afternoon were observed at LHG  
459 and NamCo sites. The high mass concentrations in the afternoon at LHG were tightly  
460 associated with the transport of aerosols advected by the prevailing up-slope winds  
461 during that time. However, the high concentration in the afternoon at NamCo might be  
462 influenced by the downward transmission of aerosols from higher layer to the ground  
463 surface, as well as enhanced aerosol plume transport from those relatively polluted  
464 western regions during the afternoon (Xu et al., 2018). A relatively complex diurnal  
465 variation pattern of total PM<sub>1</sub> was observed at the top of Mt. Waliguan, which could be  
466 attributed to the combined effects of variabilities in diffusion conditions (such as PBL  
467 height), wind directions (such as mountain-valley wind circulation), and air mass  
468 sources (such as enhanced air mass from the northeast during the afternoon, favoring  
469 the transport of polluted aerosols from industrial areas) (Zhang et al., 2019). At Motuo,  
470 the diurnal variation of PM<sub>1</sub> mass concentration was relatively stable, except for two  
471 weak peaks in the late morning and evening, which were possibly related to combustion  
472 emissions from local residents in the county. Ngari exhibited relatively high mass  
473 loadings at night, whereas low values were observed during the daytime, mainly due to  
474 the variations of PBL height. Bayanbulak, on the other hand, had relatively low and  
475 stable PM<sub>1</sub> mass throughout the entire day, primarily due to its background feature. In  
476 contrast to the remote sites, the urban site in Lhasa showed a clear diurnal variation  
477 pattern with two peaks around 8:00–9:00 and 20:00–21:00. This pattern could be  
478 attributed to strong primary aerosol emissions from vehicle exhausts, cooking, and  
479 biomass burning activities during the morning and evening times (Zhao et al., 2022).  
480 Although the diurnal variations of total PM<sub>1</sub> were mainly affected by the variabilities  
481 in mountain-valley wind circulation and PBL height in those remote sites and primary  
482 emissions in the urban site in this study, the photochemical oxidation and aqueous-  
483 phase reactions were also two important formation pathways of secondary inorganic  
484 and organic aerosol species. This could be observed clearly by those identified  
485 oxygenated OA (OOA) components at almost all the sites, which commonly showed  
486 peaks during the afternoon (Xu et al., 2018; Zhang et al., 2018; Zhang et al., 2019; Zhao



487 et al., 2022).

#### 488 **4.3 High-resolution mass spectrum and elemental ratios of organic aerosol**

489 The high-resolution mass spectrum (HRMS) and elemental ratios of OA were  
490 determined to identify the possible sources, formation and evolution mechanisms, as  
491 well as the oxidation states of these complex OA components at each site. The average  
492 O/C ratios of the OAs from the eight field campaigns were compared directly (Fig. 5a).  
493 It is evident that the average O/C ratios of OAs were generally close to or larger than  
494 1.0 at the remote sites of QOMS, Motuo, NamCo, Ngari, Waliguan, and LHG, whereas  
495 a lower O/C ratio of 0.69 was observed at Bayanbulak and an even lower O/C ratio of  
496 0.44 was observed at the urban site in Lhasa. These differences in O/C ratios were  
497 mainly attributed to the variations in OA sources and aging processes across different  
498 sites. As mentioned earlier, atmospheric aerosols in the remote sites in the TP were  
499 generally associated with long-range transport from surrounding areas, hence the OAs  
500 were generally well-mixed and highly aged during the transport from source region to  
501 the remote sites in the TP (Xu et al., 2018; Zhang et al., 2018; Zhang et al., 2019).  
502 However, local fresh OAs emitted from various residential activities such as cooking,  
503 traffic exhausts, and biomass burning predominated the total OA at urban Lhasa (Zhao  
504 et al., 2022), which ultimately led to a relatively low O/C ratio. Similar differences in  
505 O/C ratios have been observed in previous studies in China. For instance, higher O/C  
506 ratios of 0.98, 1.11, and 1.16 were measured at remote sites in Mt. Wuzhi (Zhu et al.,  
507 2016), Mt. Yulong (Zheng et al., 2017), and LHG (Xu et al., 2015), while O/C ratios of  
508 OAs were generally lower than 0.5 at most urban sites (Zhou et al., 2020). The Van  
509 Krevelen diagram (H/C versus O/C), a widely used approach to depict the changes in  
510 the elemental composition of OA resulting from atmospheric aging processing, is  
511 displayed in Fig. 5b. An overall slope of  $-0.66$  was observed for the bulk OAs across  
512 the eight field measurement campaigns in our study, which is comparable to those of  
513  $-0.58$  and  $-0.47$  obtained from different synthesized datasets from diverse field  
514 observations in previous studies (Chen et al., 2015; Zhou et al., 2020).

515 The average HRMSs of OA between the remote site (Waliguan) and the urban site  
516 (Lhasa) were directly compared to investigate the inherent difference in ion  
517 compositions (Fig. 5c). Waliguan was chosen as an example because the overall highly-  
518 aged OA nature with very similar HRMSs among the seven remote sites, as shown in  
519 Fig. S3 in the supplementary materials. It is evident that the OA HRMSs exhibited





520 distinct variations between these two types of sites. At the Waliguan site,  $m/z$  44, which  
521 is composed totally by  $\text{CO}_2^+$  and one of the most reliable markers for OOA, was the  
522 base peak (18%) in the OA HRMS. The  $\text{CO}_2^+$  and its related four ions ( $\text{CO}^+$ ,  $\text{H}_2\text{O}^+$ ,  
523  $\text{HO}^+$  and  $\text{O}^+$ ) together contributed more than 41% of the total OA signals. Additionally,  
524 the two oxygenated ion fragments ( $\text{C}_x\text{H}_y\text{O}_1^+$  and  $\text{C}_x\text{H}_y\text{O}_2^+$ ) accounted for as much as  
525 66% of the total OA signals (Fig. 5c). All these features demonstrated the overall highly  
526 oxygenated nature of OA at the remote background sites in the TP. In contrast, the OA  
527 HRMS at Lhasa was remarkably similar to those observed at most urban cities. The  
528 four  $m/z$ s value at 43, 55, 57, and 60, which are recognized as important mass spectral  
529 tracers for less oxidized OA compounds or primary emissions related to traffic, cooking,  
530 and biomass burning activities (Zhang et al., 2005a; Alfarra et al., 2007; He et al., 2010),  
531 showed significant contributions to the total OA signals in this urban site. Specifically,  
532 the ion fragment of  $\text{C}_x\text{H}_y^+$  contributed as higher as 64.5% of the total OA signal in  
533 Lhasa, whereas the two oxygenated ion fragments contributed only 33.6%. The high  
534 contribution of fresh ion fragments in the OA HRMS in Lhasa is comparable to those  
535 measured at other urban cities, such as 56% and 59% in Lanzhou (Xu et al., 2014b; Xu  
536 et al., 2016), 51.2% in Nanjing (Wang et al., 2016), and 51.2% in New York (Sun et al.,  
537 2011).

#### 538 **4.4 OA components from PMF source apportionment**

539 Source apportionments of OA were performed using PMF analysis on OA HRMS data  
540 for each field campaign. Figure 6 presents the average mass contributions of different  
541 OA components from the selected 2–4 factor solutions among the eight different field  
542 campaigns, while the specific HRMS of each OA component is displayed in Fig. S4.  
543 Due to the limited local sources but dominated sources from regional transport, only  
544 two secondary OOA factors with different oxidation degrees, namely a less oxidized  
545 OOA (LO-OOA) and a more oxidized OOA (MO-OOA), were identified during the  
546 NamCo, LHG, and Bayanbulak campaigns. On average, during the NamCo campaign,  
547 MO-OOA and LO-OOA, with average O/C ratios of 0.96 and 0.49, respectively,  
548 accounted for 59.0% and 41.0% of the total OA mass. Similarly, the Bayanbulak  
549 campaign exhibited contributions of MO-OOA (average O/C of 1.12) and LO-OOA  
550 (average O/C of 0.55) to total OA mass at 66.3% and 33.7%, respectively. However,  
551 the LHG campaign showed only 24.9% of MO-OOA and 75.1% of LO-OOA with  
552 relatively high O/C ratios of 1.29 and 1.08, respectively. Besides the two OOA factors,



553 biomass-burning-related OA (BBOA) was also widely identified in the TP regions. At  
554 QOMS, the total OA mass was composed by 42.4% of MO-OOA, 43.9% of BBOA,  
555 and 13.9% of nitrogen-containing OA (NOA), with average O/C ratios of 1.34, 0.85,  
556 and 1.10, respectively. The high O/C ratio and significant contributions from BBOA  
557 and NOA at QOMS were associated with the transport of biomass burning emissions  
558 from polluted regions in South Asia to the Himalaya and inland TP regions during the  
559 pre-monsoon season (Cong et al., 2015; Zhang et al., 2018; Kang et al., 2019a). At  
560 Waliguan, the total OA mass was composed by 34.4% of MO-OOA, 40.4% of relatively  
561 aged BBOA (agBBOA), 18.3% of BBOA, and 6.9% of hydrocarbon-like OA (HOA),  
562 with average O/C ratios of 1.42, 1.02, 0.69, and 0.33, respectively. The two BBOA  
563 components, particularly agBBOA, exhibited an enhanced contribution to total OA as  
564 the OA mass concentration increased, ranging from only ~10% to as high as 70% when  
565 OA mass varied from  $<1.0 \mu\text{g m}^{-3}$  to  $7 \mu\text{g m}^{-3}$  (Zhang et al., 2019). In addition, source  
566 analysis indicated that the high contributions of the two BBOA components at Waliguan  
567 were associated with the regional transport of biomass burning emissions from the  
568 residential areas in northeastern Waliguan (Zhang et al., 2019). At Ngari, the total OA  
569 mass was composed by 43.7% of MO-OOA, 28.5% of LO-OOA, and 27.8% of BBOA,  
570 with average O/C ratios of 1.43, 1.00, and 0.56, respectively. In comparison, the  
571 contributions of the three OA components at Motuo site were 36.9%, 46.9%, and 16.2%,  
572 with O/C ratios of 1.30, 1.11, and 0.25, respectively. The BBOA factor at Motuo  
573 exhibited relatively lower mass contribution and O/C ratio compared to those observed  
574 at QOMS, Ngari, and Waliguan, suggesting weak local source from biomass burning.  
575 Four OA factors including an OOA component with O/C ratio of 0.54 and three primary  
576 OA components, i.e., a BBOA with O/C of 0.13, a cooking-related OA (COA) with O/C  
577 of 0.12, and a HOA with O/C of 0.11, were identified at the urban site in Lhasa, which  
578 were distinctly different with those observed at above remote sites. The three primary  
579 OA components together contributed more than 60% of the total OA mass at Lhasa,  
580 suggesting the abundant primary aerosol sources from the residential activities. In  
581 addition, the BBOA contribution increased obviously (up to 36%) during a grand local  
582 festival at Lhasa, suggesting the crucial aerosol source from biomass burning during  
583 religious activities in the city (Zhao et al., 2022). In summary, distinct types of OA  
584 components with different O/C ratios were identified at different sites, indicating the  
585 different sources and oxidation states of OA in the different TP regions.



586 **4.5 Number concentrations of submicron aerosols and cloud condensation nuclei**  
587 Real-time online measurements of the size distribution of number concentration of fine  
588 particles were also conducted simultaneously using SMPS instruments during four field  
589 campaigns (QOMS, Motuo, LHG, and Lhasa). The measurement of particle number  
590 size distribution (PNSD) was not only an important auxiliary data for calibrating and  
591 verifying the accuracy of HR-ToF-AMS data, but also very useful for studying the  
592 formation and growth mechanisms of aerosol particles in the atmosphere. Figure 7a  
593 shows the high-resolution temporal variations of the PNSDs during the four field  
594 campaigns. The PNSDs varied dynamically throughout the measurement period at each  
595 site and showed distinct variations in number concentrations and size distribution  
596 pattern among the four different campaigns. On average, the total number  
597 concentrations were 709.3 and 3994.4  $\text{cm}^{-3}$  at QOMS and Lhasa, respectively, while  
598 they were 1639.2 and 1462.0  $\text{cm}^{-3}$  at Motuo and LHG. Interestingly, the difference in  
599 particle number concentrations were not consistent with those in mass concentrations  
600 measured from the HR-ToF-AMS among the four campaigns (Table 2). For example,  
601 although the  $\text{PM}_{10}$  mass concentration at Lhasa was comparable to that at QOMS (4.7  
602 versus 4.4  $\mu\text{g m}^{-3}$ ), the number concentration at Lhasa was more than five times higher  
603 than that at QOMS. This inconsistency may be related to the distinctly different size  
604 distribution at different sites. As discussed above, submicron aerosols at QOMS were  
605 overall highly aged due to the long-range transported sources from South Asia and  
606 dominated by aerosols at accumulation size mode, whereas more fresh aerosols emitted  
607 from local residential activities and dominated by aerosols of Aitken size mode were  
608 observed at Lhasa. The different sizes of submicron aerosols among the different TP  
609 regions could be further confirmed by the peak diameters in the average size  
610 distributions of mass and number concentrations (Figs. 4a and 7b). For example, the  
611 average OA mass size distributions exhibited peak diameters of 510.2 and 430.5 nm in  
612  $D_{va}$  at QOMS and Motuo, respectively, while the average number size distributions had  
613 peak diameters of 109.4 and 131.0 nm in  $D_m$  at the same sites. In contrast, Lhasa  
614 displayed peak diameters of only 228.1 nm in  $D_{va}$  and 28.9 nm in  $D_m$ .

615 New particle formation (NPF) events were also observed at a few sites in our study.  
616 Typically, an NPF event is characterized by a rapid burst in nucleation mode followed  
617 by the subsequent growth into larger particles, as defined as banana-shaped temporal  
618 developments in the PNSD (Dal Maso et al., 2005). As shown in Fig. 7a, frequent



619 banana-shaped variation patterns in the PNSD were observed at Lhasa, suggesting the  
620 frequent occurrence of NPF at this urban region. During the Lhasa campaign (27 days),  
621 a total of 10 NPF events were observed (Zhao et al., 2022). In contrast, this banana-  
622 shaped pattern was relatively rare at the other three remote sites, which might be related  
623 to their predominated transport aerosol sources, overall highly-aged states, and limited  
624 gaseous precursors.

625 Cloud condensation nuclei (CCN) is a distinct class of atmospheric aerosol particles  
626 which could be activated as cloud droplets at a certain supersaturated water vapor  
627 condition and played important roles in cloud formation, atmospheric precipitation, the  
628 regional climate, as well as the hydrological cycle (Andreae and Rosenfeld, 2008).  
629 During the TP field campaigns, real-time online measurements of CCN number  
630 concentrations were conducted at three sites, i.e., Motuo in the southeastern TP while  
631 Waliguan and LHG in the northeastern TP. Generally, the temporal variation of CCN  
632 number concentration exhibited a consistent trend with the total number concentration  
633 from the SMPS measurement or total PM<sub>1</sub> mass concentration from the HR-ToF-AMS  
634 measurement during each campaign. On average, at Motuo, the CCN number  
635 concentrations were 974.0, 1142.6, 1240.1, 1296.5, and 1337.9 cm<sup>-3</sup> at different SS  
636 values of 0.2%, 0.4%, 0.6%, 0.8%, and 1.0%, respectively. At Waliguan, relatively  
637 comparable average values of 507.0, 805.1, 1073.3, 1230.6, and 1336.6 cm<sup>-3</sup> were  
638 observed at the same SS steps, respectively. However, at LHG, these average values  
639 significantly decreased to 83.9, 344.3, 429.9, 480.8, and 516.1 cm<sup>-3</sup>, respectively (Table  
640 2). The lower CCN number concentrations at LHG compared to Waliguan and Motuo  
641 were consistent with the relatively lower PM<sub>1</sub> mass loading at the LHG site. The CCN  
642 number concentrations at the three TP sites were almost an order of magnitude lower  
643 than those observed in polluted urban atmospheres or emissions of specific combustion  
644 sources, such as 12963 cm<sup>-3</sup> (SS = 0.70%) in Wuqing, 9890 cm<sup>-3</sup> (SS = 0.86%) in  
645 Beijing (Deng et al., 2011; Gunthe et al., 2011), 7913 cm<sup>-3</sup> (SS = 0.70%) at Panyu in  
646 the Pearl River Delta, as well as 11565 cm<sup>-3</sup> (SS = 0.87%) and 10000 cm<sup>-3</sup> (SS = 0.80%)  
647 during unique biomass burning plumes (Rose et al., 2010; Zhang et al., 2020). However,  
648 our values were comparable to those (228–2150 cm<sup>-3</sup> with SS of 0.87%) measured at  
649 eight remote marine sites in the South China Sea and 941 cm<sup>-3</sup> (SS = 0.74%) in the  
650 amazon rain forest (Pöhlker et al., 2016; Atwood et al., 2017). These comparisons again  
651 highlight the overall clean atmospheric condition in the TP.



#### 652 4.6 Aerosol optical properties and light absorptions from BC and BrC

653 The optical properties of aerosol particles are crucial input parameters for accurately  
654 estimating aerosol radiative forcing in climate models. However, significant  
655 uncertainties persist due to the limited dataset in this remote region. In our project, the  
656 parameters of  $B_{scat}$ ,  $B_{abs}$ , and SSA of fine particles at 405 nm were observed during five  
657 field campaigns, i.e., QOMS, Motuo, Waliguan, Ngari, and Lhasa, to explore the  
658 differences in aerosol optical properties at different TP regions. On average, the  $B_{scat}$   
659 and  $B_{abs}$  at 405 nm during the five campaigns were 121.9, 44.9, 36.3, 8.9, and 2.1  $\text{Mm}^{-1}$   
660 and 10.8, 7.0, 4.1, 3.6, and 1.9  $\text{Mm}^{-1}$ , respectively, which finally resulted in average  
661 SSA values of 0.89, 0.83, 0.86, 0.67, and 0.52, correspondingly (Fig. 8a and Table 2).  
662 These  $B_{scat}$  and  $B_{abs}$  values at the five TP sites were both significantly lower than those  
663 reported at various urban sites in China, such as 459.5 and 47.2  $\text{Mm}^{-1}$ , respectively, at  
664 630 nm in Beijing (Xie et al., 2019), 272 and 31  $\text{Mm}^{-1}$ , respectively, at 532 nm in Xi'an  
665 (Zhu et al., 2015), and 418 and 91  $\text{Mm}^{-1}$ , respectively, at 540 nm in Guangzhou  
666 (Andreae et al., 2008), once again suggesting the overall clean atmospheric condition  
667 in the TP. Although the  $\text{PM}_{10}$  mass at QOMS was comparable to or lower than those at  
668 the other four sites, the highest  $B_{scat}$ ,  $B_{abs}$ , and SSA values were observed at QOMS.  
669 These results may be attributed to the differences in aerosol chemical compositions and  
670 mass scattering and absorbing efficiencies. In contrast, Lhasa exhibited a significantly  
671 lower SSA compared to the other four remote sites, suggesting a prevalence of fresh  
672 aerosols in the urban area. On the other hand, aerosols at the four remote sites were  
673 highly aged, which resulted in significant photobleaching in BrC chromophores and an  
674 obvious decrease in their light absorptivity at these sites.

675 In this study, real-time online measurements of particle  $B_{abs}$  at seven fixed wavelengths  
676 (370–950 nm) were also conducted using an aethalometer at QOMS, NamCo, and  
677 Waliguan, respectively, to explore the regional difference in aerosol absorption  
678 properties in the different TP regions. Overall, the multi-wavelength  $B_{abs}$  decreased  
679 significantly with the increasing wavelength during all the three measurement  
680 campaigns, with fitting AAE values to be 1.73, 1.28, and 1.12, respectively (Fig. 8b).  
681 The average  $B_{abs}$  at the shortest wavelength of 370 nm was 13.40, 3.25, and 2.66  $\text{Mm}^{-1}$   
682 at the three sites, respectively (Table 2). Although a relatively low  $\text{PM}_{10}$  mass was  
683 observed at QOMS, the  $B_{abs}$  at 370 nm was five times higher than that at Waliguan,  
684 mainly as a result of the higher contribution of light-absorbing aerosol components in



685 the southern TP regions. For example, OA and BC together contributed nearly 80% of  
686 the total  $PM_{10}$  at QOMS, whereas this contribution decreased to only 37.5% at Waliguan.  
687 The obviously higher AAE at QOMS also suggested a dominant light-absorbing  
688 contribution from BrC or the significant lensing effect of non-BC materials coated on  
689 BC at this southern site (Zhang et al., 2021). As shown in the inserted plots in Fig. 8b,  
690 both BC and BrC components showed significant decrease of particle  $B_{abs}$  ( $B_{abs,BC}$  and  
691  $B_{abs,BrC}$ ) with increasing wavelength, but their contributions to total  $B_{abs}$  ( $fB_{abs,BC}$  and  
692  $fB_{abs,BrC}$ ) varied inversely. BC was the primary light-absorbing component at all the  
693 three sites, contributing 66.9%, 78.7%, and 77.6% to the total  $B_{abs}$  at 370 nm at QOMS,  
694 NamCo, and Waliguan sites, respectively, and its contribution increased apparently with  
695 longer wavelengths (Table 2). BrC showed more significant contributions to total  $B_{abs}$   
696 at shorter wavelengths. For example, the average  $B_{abs,BrC}$  at 370 nm were 4.42, 0.69,  
697 and  $0.60 \text{ Mm}^{-1}$  at the three sites, respectively, which finally contributed 33.1%, 21.3%,  
698 and 22.4% of the total  $B_{abs}$ . The significantly higher values of total  $B_{abs}$ ,  $B_{abs,BC}$ ,  $B_{abs,BrC}$ ,  
699 and  $fB_{abs,BrC}$  in the southern TP region could be related to the important contributions  
700 of light-absorbing CAs from transported biomass burning emissions (Xu et al., 2020,  
701 2022).

#### 702 4.7 Estimation of aerosol radiative forcing in the different TP regions

703 Atmospheric aerosols have been found to significantly impact the Earth's climate  
704 systems through affecting solar radiation and exerting a positive forcing on the energy  
705 budget (Bond and Bergstrom, 2006). In this study, aerosol direct radiative forcings  
706 (DRF) caused by BC, organic carbon (OC), and water-soluble ions (WSIs) are  
707 estimated, respectively, by the widely used Santa Barbara DISORT (Discrete Ordinate  
708 Radiative Transfer) Atmospheric Radiative Transfer (SBDART) model (Ricchiuzzi et  
709 al., 1998). A detailed introduction and operation process of this model are described in  
710 Text S6 in the supplementary material. Since the model's performance is evaluated and  
711 calibrated by comparing the values with measurements from the Aethalometer and PAX  
712 instruments, the aerosol DRF estimations are limited to the three sites of QOMS,  
713 NamCo, and Waliguan, which have both online measurements from the aforementioned  
714 instruments. Furthermore, these three sites are located in the southern, central, and  
715 northern regions of the TP, respectively, which enables us to explore the regional  
716 variations in aerosol DRF across different TP regions.

717 Figure 9 presents the modelled DRFs caused by BC, OC, and WSIs during the three



718 campaigns. BC exhibited a significant warming effect at the top of the atmosphere, with  
719 average DRF values of  $+2.5 \pm 0.5$ ,  $+2.1 \pm 0.1$ , and  $+1.9 \pm 0.1 \text{ W m}^{-2}$  during the QOMS,  
720 Waliguan, and NamCo campaign, respectively. In contrast, a noticeable cooling effect  
721 caused by BC was observed at the earth's surface with average DRF values of  $-4.7 \pm$   
722  $0.8$ ,  $-4.1 \pm 0.2$ , and  $-3.7 \pm 0.1 \text{ W m}^{-2}$  across the three campaigns. The combination of  
723 warming effect at the top of the atmosphere and cooling effect at the earth's surface  
724 resulted in significantly high net atmospheric forcings by BC, amounting to  $+7.3 \pm 1.2$ ,  
725  $+6.2 \pm 0.3$ , and  $+5.6 \pm 0.2 \text{ W m}^{-2}$  during the QOMS, Waliguan, and NamCo campaigns,  
726 respectively. These findings suggest the important radiative effect caused by BC in the  
727 TP, especially in the southern TP region, which was significantly influenced by the  
728 long-range transported biomass burning emission from South Asia. For OC and WSIs,  
729 cooling effects were observed at both the top of the atmosphere and the earth's surface,  
730 characterized by negative and low average DRFs. Consequently, the net atmospheric  
731 forcings for OC and WSIs were significantly lower compared to BC across the three  
732 campaigns, with values of  $+2.0 \pm 1.2$ ,  $+0.7 \pm 0.2$ , and  $+0.9 \pm 0.7 \text{ W m}^{-2}$  for OC, and  
733  $+1.9 \pm 0.8$ ,  $+1.4 \pm 0.6$ , and  $+1.2 \pm 0.2 \text{ W m}^{-2}$  for WSIs at QOMS, Waliguan and NamCo,  
734 respectively. Interestingly, at QOMS, the average atmospheric DRF of OC accounted  
735 for 27.3% of that of BC, whereas at Waliguan and NamCo, the fractions were only 11.1%  
736 and 15.7%, respectively. The higher atmospheric DRF observed at QOMS suggests a  
737 dominant contribution from light-absorbing BC and BrC aerosols, compared to  
738 Waliguan and NamCo. It was worth noting that the simulations of DRF effects in this  
739 study were only conducted at three specific sites during limited periods. Therefore,  
740 long-term comprehensive measurements and DRF simulations over the entire TP  
741 regions under different seasons are needed in the future.

#### 742 **4.8 Long-range transport of aerosols from surrounding areas**

743 To further understand the potential sources and specific transport pathways of air  
744 masses at each site, particularly for those remote sites where regional transport  
745 dominated, three- or five-days air mass back trajectories were calculated during each  
746 measurement period at an ending height of 500 m above ground level every 6h using  
747 the Hybrid Single Particle Lagrangian Integrated Trajectory (HYSPLIT) model  
748 (Draxler and Rolph, 2003). Figure 10 display the average backward trajectory clusters  
749 during all the eight field campaigns and the major trajectory clusters at each site are  
750 marked with large solid circles in different colors.



751 In general, distinct air mass sources were identified among the different TP regions. The  
752 five sites (QOMS, Motuo, Lhasa, NamCo, and Ngari) located in the southern or south-  
753 central part of the TP generally showed dominant air mass sources from the south or  
754 southwest with different transport distances and pathways during their measurement  
755 periods in pre-monsoon season. For example, during the QOMS campaign, 38% of the  
756 air masses originated from the west, covering a considerably long transport distance,  
757 while another 40% was originated from the southwest, covering a relatively shorter  
758 distance. In the Motuo campaign, two major clusters were both from the southwest, but  
759 their transport distances were distinctly different (77% at shorter distance compared to  
760 only 13% at a longer distance). Similarly, during the NamCo campaign, two different  
761 major clusters with comparable contributions (37% and 34%) and transport distances,  
762 but different transport pathways, were found from the south. The Ngari campaign also  
763 observed similar transport distances, with 56% of the air masses originating from  
764 southwest and 26% from south of the site. These air mass clusters originating from the  
765 south of the TP generally traverse heavy polluted regions in South Asia, such as the  
766 Indo-Gangetic Plain, Nepal, and Bangladesh, carrying significant amounts of polluted  
767 aerosols, particularly the biomass-burning-related emissions from the source origins to  
768 the inland of the TP. In contrast, air masses at the northern sites were primarily  
769 influenced by the prevailing Westerlies wind and East Asian monsoon during the  
770 summer season measurement periods. In the Bayanbulak campaign, the major air  
771 masses were all originated from the west of the site with varying transport distances  
772 (i.e., 69% in relatively shorter distance versus 18% in a longer distance). During the  
773 LHG campaign, the air masses originated from the northwest of the site with 63% in  
774 longer transport distance but 27% in shorter distance. For the Waliguan campaign, the  
775 air mass clusters originated from two distinctly different directions. The majority of the  
776 air masses (57%) came from the northeast of the site covering a relatively shorter  
777 distance and faster transport speed, while the remaining clusters originated from the  
778 west and northwest of the site covering significantly longer distances. In summary,  
779 significant differences in air mass sources and transport pathways were identified  
780 among the different TP regions, particularly between the southern and the northern TP  
781 regions. These differences are the primary factors contributing to the significantly  
782 different physiochemical and optical properties of aerosols in the different TP regions.

## 783 **5 Dataset limitations and applications**





784 Our dataset was achieved from multiple short-term intensive field observations  
785 conducted at eight different sites of the TP during their high-mass-loading periods  
786 utilizing a suite of high-resolution online instruments. However, it is important to  
787 acknowledge that our dataset has certain limitations due to objective restrictions that  
788 were quite challenging to overcome in these remote regions.

789 The primary limitation revolves around the short and inconsistent measurement periods  
790 across different observational years and seasons at different sites. This limitation  
791 hinders the ability to make a robust comparison of aerosol properties across the vast TP  
792 region, ascertain long-term and seasonal variation characteristics, and apply the current  
793 data and findings to other different seasons. The harsh natural environments,  
794 challenging weather conditions, limited logistical support, sole availability of our high-  
795 resolution instruments, and the stringent instrumental requirements (e.g., the need for  
796 comprehensive field stations with uninterrupted and stable power supply) were the most  
797 significant challenges we faced during our field observations in these remote TP regions.  
798 It is worth noting that online HR-ToF-AMS observations, such as the ones we  
799 conducted, are predominantly short-term and intense observations carried out  
800 worldwide due to the stability and its challenging maintenance during long-term  
801 measurement. The short-term intensive measurement can well capture and characterize  
802 the dynamic evolution of aerosol properties at a high-time-resolution (Jimenez et al.,  
803 2009; Li et al., 2017). Until now, long-term high-time-resolution observation utilizing  
804 HR-ToF-AMS have rarely been conducted, even at urban sites with relatively favorable  
805 observational environments and logistic support compared to our remote TP sites.  
806 Consequently, performing continuous long-term observations or simultaneous  
807 comparison at multiple sites in these high-altitude remote and challenging TP regions,  
808 without stable power supply, is nearly impossible.

809 However, our team has made significant efforts to conduct the comprehensive  
810 observation project over the past ten years, aiming to study the regional differences in  
811 aerosol sources and properties across the different TP regions. The dataset generated  
812 from our project represents the first and sole high-time-resolution dataset focusing on  
813 atmospheric aerosol physicochemical and optical properties, coring the most part of the  
814 TP. The applications of this dataset in atmospheric science can be summarized as  
815 follows: firstly, the high-time-resolution observations offer crucial advantages  
816 understanding the rapid evolution and diurnal variations of aerosol properties during a



817 short period or special event. Additionally, these observations are valuable for model  
818 simulation and verification, as they provide sufficient data points. Such advantages are  
819 not achievable with traditional off-line samplings, which have low time resolutions  
820 ranging from days to weeks. Secondly, the eight sites included in our project effectively  
821 represent a wide range of the TP. This is particularly noteworthy considering the limited  
822 availability of observational stations on the plateau. Furthermore, these sites provide  
823 excellent opportunities for comparing aerosol sources and properties among different  
824 types of sites with varying altitudes, land covers, surrounding environments, human  
825 activities, and influences from large-scale atmospheric circulations. Thirdly, our  
826 observations encompass a wide range of aerosol physical, chemical, and optical  
827 parameters, including aerosol mass loadings, chemical compositions, size distribution,  
828 diurnal variations, number concentrations, light scattering and absorption coefficients,  
829 and so on. This comprehensive dataset is crucial for a thorough understanding of aerosol  
830 properties in the TP regions. Overall, it is worth noting that until now, similar online  
831 observational aerosol datasets focusing on multiple parameters with at least hourly-  
832 scale resolution at various sites in the diverse TP regions had been rarely reported.

## 833 **6 Data availability**

834 The high-resolution online measurement datasets, encompassing aerosol physical,  
835 chemical, and optical properties over the Tibetan Plateau and its surroundings in our  
836 observation project have been released and are now available for download from the  
837 National Cryosphere Desert Data Center  
838 (<https://doi.org/10.12072/ncdc.NIEER.db2200.2022>). These datasets are provided in an  
839 Excel file comprising eight worksheets. The first sheet of the Excel file contains a  
840 concise description of the dataset, including the dataset name, observation stations,  
841 sampling periods, online instruments used, and corresponding references. The  
842 remaining seven sheets present the high-resolution measurement data obtained from the  
843 online instruments employed during the eight campaigns. These instruments include  
844 HR-ToF-AMS, SMPS, PAX, aethalometer, and CCN-100.

## 845 **7 Conclusions**

846 A comprehensive dataset including aerosol physicochemical and optical properties,  
847 especially the high-resolution size-resolved chemical characteristics and sources of  
848 submicron aerosols, conducted through real-time online measurements at different sites



849 of the TP and its surroundings is presented in this study. The objective of this study is  
850 to elucidate the mass concentration level of atmospheric aerosols in this isolated  
851 background region and identify regional variations in aerosol sources, as well as  
852 physicochemical and optical properties among different TP regions. Ultimately, these  
853 valuable data will significantly contribute to accurately simulating the radiative forcing  
854 and other potential impacts of atmospheric aerosols in this remote region in future  
855 climatic models.

856 A total of eight aerosol field measurements were conducted at QOMS, Motuo, NamCo,  
857 Ngari, Waliguan, LHG, Bayanbulak, and Lhasa in the different regions of TP and its  
858 surroundings by deploying multiple online instruments, including HR-ToF-AMS,  
859 SMPS, PAX, Aethalometer, and CCN-100. The collected datasets provide the temporal  
860 and diurnal variations as well as the size distribution patterns of  $PM_{10}$  chemical  
861 compositions, the standard high-resolution mass spectra and temporal variations of OA  
862 components, the temporal variations of particle number size distribution, particle light  
863 scattering and absorption coefficients, particle light absorptions from different CAs of  
864 BC and BrC, and CCN number concentrations at different supersaturation in each  
865 campaign.

866 The datasets provide valuable insights into the regional variations in aerosol properties  
867 and sources. In the southern TP region, atmospheric aerosols were found to be primarily  
868 influenced by biomass burning emissions from polluted regions in South Asia, which  
869 resulted in high mass contributions ( $>70\%$ ) of CAs and overall neutralized  $PM_{10}$ , as well  
870 as an enhanced light absorption capability of the light-absorbing BC and BrC. In  
871 contrast, in the northern TP, secondary inorganic species, particularly sulfate,  
872 contributed significantly to total  $PM_{10}$  due to the regional transport of anthropogenic  
873 aerosol and gaseous precursor emissions from urban areas in northwestern China.  
874 Furthermore, in contrast to the well-mixed, highly-aged, and regionally transported  
875 aerosols observed in the remote sites, atmospheric aerosols in the urban Lhasa were  
876 mainly originated from local primary sources such as cooking, traffic vehicle exhausts,  
877 and biofuel combustion during the residential activities. Consequently, these aerosol  
878 particles were relatively fresh, characterized by small size and low oxidation degree,  
879 but exhibited a high frequency of NPF origins.

## 880 **Appendix A: Main Abbreviations**



TP	Tibetan Plateau
HR-ToF-AMS	high-resolution time-of-flight aerosol mass spectrometer
SMPS	scanning mobility particle sizer
PAX	photo-acoustic extinctions
CCN	cloud condensation nuclei
SS	supersaturation
PM <sub>1</sub>	submicron aerosol
BC	black carbon
BrC	brown carbon
OA	organic aerosol
SNA	sulfate, nitrate, and ammonium
$D_m$	mobility diameter
$D_{va}$	aerodynamic diameter
CE	collection efficiency
HRMS	high-resolution mass spectrum
PBL	planetary boundary layer
O/C	oxygen-to-carbon ratio
H/C	hydrogen-to-carbon ratio
N/C	nitrogen-to-carbon ratio
OM/OC	organic matter-to-organic carbon ratio
PMF	positive matrix factorization
OOA	oxygenated organic aerosol
LO-OOA	less oxidized oxygenated organic aerosol
MO-OOA	more oxidized oxygenated organic aerosol
BBOA	biomass-burning-related organic aerosol
agBBOA	aged biomass-burning-related organic aerosol
NOA	nitrogen-containing organic aerosol
HOA	traffic-related hydrocarbon-like organic aerosol
COA	cooking-related organic aerosol
PNSD	particle number size distribution
NPF	new particle formation
$B_{scat}$	light scattering coefficient
$B_{abs}$	light absorption coefficient
$B_{ext}$	light extinction coefficient
SSA	single scattering albedo
AAE	absorption Ångström exponents
$B_{abs,BC}$	light absorption coefficient from BC
$B_{abs,BrC}$	light absorption coefficient from BrC
OC	organic carbon
WSIs	water-soluble ions
DRF	direct radiative forcing

881 **Author Contributions.** JX designed the study, XZ, WZ, and JX wrote the manuscript.  
882 JX and SK organized and supervised the field measurement campaigns, JX, XZ, WZ,  
883 LZ, MZ, JS, JShi, YL, CX, YT, KL, XG, and QZ conducted the field measurements,  
884 JX, XZ, WZ, and YT analyzed the data. All authors reviewed and commented on the  
885 final form of the manuscript.



886 **Competing interests.** The authors declared that they have no competing interests.

887 **Acknowledgements.** We appreciate all our colleagues and collaborators who  
888 participated the aerosol field measurements, maintained the instruments, analyzed the  
889 data, and commented on the manuscript. We also show great thanks to all the  
890 observation stations in this study for their logistical supports with the field campaigns.

891 **Financial support.** This work was supported by the National Natural Science  
892 Foundation of China (41977189, 41771079, 41805106), the Second Tibetan Plateau  
893 Scientific Expedition and Research program (STEP) (2019QZKK0605), the Strategic  
894 Priority Research Program of Chinese Academy of Sciences, Pan-Third Pole  
895 Environment Study for a Green Silk Road (Pan-TPE) (XDA20040501), the State Key  
896 Laboratory of Cryospheric Sciences Scientific Research Foundation (SKLCS-ZZ-  
897 2023), and the Chinese Academy of Sciences Hundred Talents Program.

## 898 References

- 899 Aiken, A. C., Salcedo, D., Cubison, M. J., Huffman, J. A., DeCarlo, P. F., Ulbrich, I. M., Docherty, K. S.,  
900 Sueper, D., Kimmel, J. R., Worsnop, D. R., Trimborn, A., Northway, M., Stone, E. A., Schauer, J. J.,  
901 Volkamer, R. M., Fortner, E., de Foy, B., Wang, J., Laskin, A., Shutthanandan, V., Zheng, J., Zhang,  
902 R., Gaffney, J., Marley, N. A., Paredes-Miranda, G., Arnott, W. P., Molina, L. T., Sosa, G., and Jimenez,  
903 J. L.: Mexico City aerosol analysis during MILAGRO using high resolution aerosol mass spectrometry  
904 at the urban supersite (T0) – Part 1: Fine particle composition and organic source apportionment,  
905 *Atmos. Chem. Phys.*, 9, 6633-6653, <https://doi.org/10.5194/acp-9-6633-2009>, 2009.
- 906 Alfarrá, M. R., Prevot, A. S. H., Szidat, S., Sandradewi, J., Weimer, S., Lanz, V. A., Schreiber, D., Mohr,  
907 M., and Baltensperger, U.: Identification of the mass spectral signature of organic aerosols from wood  
908 burning emissions, *Environ. Sci. Technol.*, 41, 5770-5777, <https://doi.org/10.1021/es062289b>, 2007.
- 909 An, Y., Xu, J., Feng, L., Zhang, X., Liu, Y., Kang, S., Jiang, B., and Liao, Y.: Molecular characterization  
910 of organic aerosol in the Himalayas: insight from ultra-high-resolution mass spectrometry, *Atmos.*  
911 *Chem. Phys.*, 19, 1115-1128, <https://doi.org/10.5194/acp-19-1115-2019>, 2019.
- 912 Andreae, M. O., and Rosenfeld, D.: Aerosol–cloud–precipitation interactions. Part 1. The nature and  
913 sources of cloud-active aerosols, *Earth-Science Reviews*, 89, 13-41,  
914 <https://doi.org/10.1016/j.earscirev.2008.03.001>, 2008.
- 915 Andreae, M. O., Schmid, O., Yang, H., Chand, D., Zhen Yu, J., Zeng, L.-M., and Zhang, Y.-H.: Optical  
916 properties and chemical composition of the atmospheric aerosol in urban Guangzhou, China, *Atmos.*  
917 *Environ.*, 42, 6335-6350, <https://doi.org/10.1016/j.atmosenv.2008.01.030>, 2008.
- 918 Atwood, S. A., Reid, J. S., Kreidenweis, S. M., Blake, D. R., Jonsson, H. H., Lagrosas, N. D., Xian, P.,  
919 Reid, E. A., Sessions, W. R., and Simpas, J. B.: Size-resolved aerosol and cloud condensation nuclei  
920 (CCN) properties in the remote marine South China Sea – Part 1: Observations and source  
921 classification, *Atmos. Chem. Phys.*, 17, 1105-1123, <https://doi.org/10.5194/acp-17-1105-2017>, 2017.
- 922 Bonasoni, P., Laj, P., Marinoni, A., Sprenger, M., Angelini, F., Arduini, J., Bonafè, U., Calzolari, F.,  
923 Colombo, T., Decesari, S., Di Biagio, C., di Sarra, A. G., Evangelisti, F., Duchi, R., Facchini, M. C.,  
924 Fuzzi, S., Gobbi, G. P., Maione, M., Panday, A., Roccatò, F., Sellegri, K., Venzac, H., Verza, G. P.,  
925 Villani, P., Vuillermoz, E., and Cristofanelli, P.: Atmospheric Brown Clouds in the Himalayas: first  
926 two years of continuous observations at the Nepal Climate Observatory-Pyramid (5079 m), *Atmos.*  
927 *Chem. Phys.*, 10, 7515-7531, <https://doi.org/10.5194/acp-10-7515-2010>, 2010.
- 928 Bond, T. C., and Bergstrom, R. W.: Light absorption by carbonaceous particles: An investigative review,  
929 *Aerosol Sci. Technol.*, 40, 27-67, <https://doi.org/10.1080/02786820500421521>, 2006.
- 930 Canagaratna, M. R., Jimenez, J. L., Kroll, J. H., Chen, Q., Kessler, S. H., Massoli, P., Hildebrandt Ruiz,  
931 L., Fortner, E., Williams, L. R., Wilson, K. R., Surratt, J. D., Donahue, N. M., Jayne, J. T., and Worsnop,



- 932 D. R.: Elemental ratio measurements of organic compounds using aerosol mass spectrometry:  
933 characterization, improved calibration, and implications, *Atmos. Chem. Phys.*, 15, 253-272,  
934 <https://doi.org/10.5194/acp-15-253-2015>, 2015.
- 935 Cao, J., Xu, B., He, J., Liu, X., Han, Y., Wang, G., and Zhu, C.: Concentrations, seasonal variations, and  
936 transport of carbonaceous aerosols at a remote Mountainous region in western China, *Atmos. Environ.*,  
937 43, 4444-4452, <https://doi.org/10.1016/j.atmosenv.2009.06.023>, 2009.
- 938 Chen, F., Ding, L., Piao, S., Zhou, T., Xu, B., Yao, T., and Li, X.: The Tibetan Plateau as the engine for  
939 Asian environmental change: the Tibetan Plateau Earth system research into a new era, *Science*  
940 *Bulletin*, 66, 1263-1266, <https://doi.org/10.1016/j.scib.2021.04.017>, 2021.
- 941 Chen, P., Kang, S., Li, C., Zhang, Q., Guo, J., Tripathee, L., Zhang, Y., Li, G., Gul, C., Cong, Z., Wan,  
942 X., Niu, H., Panday, A. K., Rupakheti, M., and Ji, Z.: Carbonaceous aerosol characteristics on the Third  
943 Pole: A primary study based on the Atmospheric Pollution and Cryospheric Change (APCC) network,  
944 *Environ. Pollut.*, 253, 49-60, <https://doi.org/10.1016/j.envpol.2019.06.112>, 2019.
- 945 Chen, Q., Heald, C. L., Jimenez, J. L., Canagaratna, M. R., Zhang, Q., He, L. Y., Huang, X. F.,  
946 Campuzano-Jost, P., Palm, B. B., Poulain, L., Kuwata, M., Martin, S. T., Abbatt, J. P. D., Lee, A. K.  
947 Y., and Liggio, J.: Elemental composition of organic aerosol: The gap between ambient and laboratory  
948 measurements, *Geophys. Res. Lett.*, 42, 4182-4189, <https://doi.org/10.1002/2015gl063693>, 2015.
- 949 Cong, Z., Kang, S., Kawamura, K., Liu, B., Wan, X., Wang, Z., Gao, S., and Fu, P.: Carbonaceous  
950 aerosols on the south edge of the Tibetan Plateau: concentrations, seasonality and sources, *Atmos.*  
951 *Chem. Phys.*, 15, 1573-1584, <https://doi.org/10.5194/acp-15-1573-2015>, 2015.
- 952 Cui, Y. Y., Liu, S., Bai, Z., Bian, J., Li, D., Fan, K., McKeen, S. A., Watts, L. A., Ciciora, S. J., and Gao,  
953 R.-S.: Religious burning as a potential major source of atmospheric fine aerosols in summertime Lhasa  
954 on the Tibetan Plateau, *Atmos. Environ.*, 181, 186-191,  
955 <https://doi.org/10.1016/j.atmosenv.2018.03.025>, 2018.
- 956 Dal Maso, M., Kulmala, M., Riipinen, I., Wagner, R., Hussein, T., Aalto, P. P., and Lehtinen, K. E. J.:  
957 Formation and growth of fresh atmospheric aerosols: eight years of aerosol size distribution data from  
958 SMEAR II, Hyytiälä, Finland, *Boreal Environ. Res.*, 10, 323-336, 2005.
- 959 Deng, Z. Z., Zhao, C. S., Ma, N., Liu, P. F., Ran, L., Xu, W. Y., Chen, J., Liang, Z., Liang, S., Huang, M.  
960 Y., Ma, X. C., Zhang, Q., Quan, J. N., Yan, P., Henning, S., Mildnerberger, K., Sommerhage, E., Schäfer,  
961 M., Stratmann, F., and Wiedensohler, A.: Size-resolved and bulk activation properties of aerosols in  
962 the North China Plain, *Atmos. Chem. Phys.*, 11, 3835-3846, <https://doi.org/10.5194/acp-11-3835-2011>,  
963 2011.
- 964 Draxler, R. R., and Rolph, G. D.: HYSPLIT (HYbrid Single-Particle Lagrangian Integrated Trajectory)  
965 model access via NOAA ARL READY website (<http://www.arl.noaa.gov/ready/hysplit4.html>). in,  
966 NOAA Air Resources Laboratory, Silver Spring, MD, USA, 2003.
- 967 Du, W., Sun, Y. L., Xu, Y. S., Jiang, Q., Wang, Q. Q., Yang, W., Wang, F., Bai, Z. P., Zhao, X. D., and  
968 Yang, Y. C.: Chemical characterization of submicron aerosol and particle growth events at a national  
969 background site (3295 m a.s.l.) on the Tibetan Plateau, *Atmos. Chem. Phys.*, 15, 10811-10824,  
970 <https://doi.org/10.5194/acp-15-10811-2015>, 2015.
- 971 Duan, A. M., and Wu, G. X.: Role of the Tibetan Plateau thermal forcing in the summer climate patterns  
972 over subtropical Asia, *Clim. Dyn.*, 24, 793-807, <https://doi.org/10.1007/s00382-004-0488-8>, 2005.
- 973 Freney, E. J., Sellegrì, K., Canonaco, F., Boulon, J., Hervo, M., Weigel, R., Pichon, J. M., Colomb, A.,  
974 Prévôt, A. S. H., and Laj, P.: Seasonal variations in aerosol particle composition at the puy-de-Dôme  
975 research station in France, *Atmos. Chem. Phys.*, 11, 13047-13059, <https://doi.org/10.5194/acp-11-13047-2011>, 2011.
- 976 Fröhlich, R., Cubison, M. J., Slowik, J. G., Bukowiecki, N., Canonaco, F., Croteau, P. L., Gysel, M.,  
977 Henne, S., Herrmann, E., Jayne, J. T., Steinbacher, M., Worsnop, D. R., Baltensperger, U., and Prévôt,  
978 A. S. H.: Fourteen months of on-line measurements of the non-refractory submicron aerosol at the  
979 Jungfraujoch (3580 m a.s.l.) – chemical composition, origins and organic aerosol sources, *Atmos.*  
980 *Chem. Phys.*, 15, 11373-11398, <https://doi.org/10.5194/acp-15-11373-2015>, 2015.
- 981 Gunthe, S. S., Rose, D., Su, H., Garland, R. M., Achtert, P., Nowak, A., Wiedensohler, A., Kuwata, M.,  
982 Takegawa, N., Kondo, Y., Hu, M., Shao, M., Zhu, T., Andreae, M. O., and Pöschl, U.: Cloud  
983 condensation nuclei (CCN) from fresh and aged air pollution in the megacity region of Beijing, *Atmos.*  
984 *Chem. Phys.*, 11, 11023-11039, <https://doi.org/10.5194/acp-11-11023-2011>, 2011.
- 985 He, L. Y., Lin, Y., Huang, X. F., Guo, S., Xue, L., Su, Q., Hu, M., Luan, S. J., and Zhang, Y. H.:  
986 Characterization of high-resolution aerosol mass spectra of primary organic aerosol emissions from  
987 Chinese cooking and biomass burning, *Atmos. Chem. Phys.*, 10, 11535-11543,  
988 <https://doi.org/10.5194/acp-10-11535-2010>, 2010.
- 989 Jimenez, J. L., Canagaratna, M. R., Donahue, N. M., Prevot, A. S., Zhang, Q., Kroll, J. H., DeCarlo, P.  
990 F., Allan, J. D., Coe, H., Ng, N. L., Aiken, A. C., Docherty, K. S., Ulbrich, I. M., Grieshop, A. P.,



- 992 Robinson, A. L., Duplissy, J., Smith, J. D., Wilson, K. R., Lanz, V. A., Hueglin, C., Sun, Y. L., Tian, J.,  
993 Laaksonen, A., Raatikainen, T., Rautiainen, J., Vaattovaara, P., Ehn, M., Kulmala, M., Tomlinson, J.  
994 M., Collins, D. R., Cubison, M. J., Dunlea, E. J., Huffman, J. A., Onasch, T. B., Alfarra, M. R.,  
995 Williams, P. I., Bower, K., Kondo, Y., Schneider, J., Drewnick, F., Borrmann, S., Weimer, S.,  
996 Demerjian, K., Salcedo, D., Cottrell, L., Griffin, R., Takami, A., Miyoshi, T., Hatakeyama, S., Shimono,  
997 A., Sun, J. Y., Zhang, Y. M., Dzepina, K., Kimmel, J. R., Sueper, D., Jayne, J. T., Herndon, S. C.,  
998 Trimborn, A. M., Williams, L. R., Wood, E. C., Middlebrook, A. M., Kolb, C. E., Baltensperger, U.,  
999 and Worsnop, D. R.: Evolution of organic aerosols in the atmosphere, *Science*, 326, 1525-1529,  
1000 <https://doi.org/10.1126/science.1180353>, 2009.
- 1001 Kang, S., Xu, Y., You, Q., Flügel, W.-A., Pepin, N., and Yao, T.: Review of climate and cryospheric  
1002 change in the Tibetan Plateau, *Environ. Res. Lett.*, 5, 015101, [https://doi.org/10.1088/1748-](https://doi.org/10.1088/1748-9326/5/1/015101)  
1003 [9326/5/1/015101](https://doi.org/10.1088/1748-9326/5/1/015101), 2010.
- 1004 Kang, S., Chen, P., Li, C., Liu, B., and Cong, Z.: Atmospheric Aerosol Elements over the Inland Tibetan  
1005 Plateau: Concentration, Seasonality, and Transport, *Aerosol Air Qual. Res.*, 16, 789-800,  
1006 <https://doi.org/10.4209/aaqr.2015.05.0307>, 2016.
- 1007 Kang, S., Cong, Z., Wang, X., Zhang, Q., Ji, Z., Zhang, Y., and Xu, B.: The transboundary transport of  
1008 air pollutants and their environmental impacts on Tibetan Plateau, *Chin. Sci. Bull.*, 64, 2876-2884,  
1009 <https://doi.org/10.1360/tb-2019-0135>, 2019a.
- 1010 Kang, S., Zhang, Q., Qian, Y., Ji, Z., Li, C., Cong, Z., Zhang, Y., Guo, J., Du, W., Huang, J., You, Q.,  
1011 Panday, A. K., Rupakheti, M., Chen, D., Gustafsson, Ö., Thiemens, M. H., and Qin, D.: Linking  
1012 atmospheric pollution to cryospheric change in the Third Pole region: current progress and future  
1013 prospects, *Natl. Sci. Rev.*, 6, 796-809, <https://doi.org/10.1093/nsr/nwz031>, 2019b.
- 1014 Kang, S., Zhang, Y., Chen, P., Guo, J., Zhang, Q., Cong, Z., Kaspari, S., Tripathee, L., Gao, T., Niu, H.,  
1015 Zhong, X., Chen, X., Hu, Z., Li, X., Li, Y., Neupane, B., Yan, F., Rupakheti, D., Gul, C., Zhang, W.,  
1016 Wu, G., Yang, L., Wang, Z., and Li, C.: Black carbon and organic carbon dataset over the Third Pole,  
1017 *Earth System Science Data*, 14, 683-707, <https://doi.org/10.5194/essd-14-683-2022>, 2022.
- 1018 Kopacz, M., Mauzerall, D. L., Wang, J., Leibensperger, E. M., Henze, D. K., and Singh, K.: Origin and  
1019 radiative forcing of black carbon transported to the Himalayas and Tibetan Plateau, *Atmos. Chem.*  
1020 *Phys.*, 11, 2837-2852, <https://doi.org/10.5194/acp-11-2837-2011>, 2011.
- 1021 Lau, K. M., Kim, M. K., and Kim, K. M.: Asian summer monsoon anomalies induced by aerosol direct  
1022 forcing: the role of the Tibetan Plateau, *Clim. Dyn.*, 26, 855-864, [https://doi.org/10.1007/s00382-006-](https://doi.org/10.1007/s00382-006-0114-z)  
1023 [0114-z](https://doi.org/10.1007/s00382-006-0114-z), 2006.
- 1024 Li, C., Bosch, C., Kang, S., Andersson, A., Chen, P., Zhang, Q., Cong, Z., Chen, B., Qin, D., and  
1025 Gustafsson, O.: Sources of black carbon to the Himalayan-Tibetan Plateau glaciers, *Nat. Commun.*, 7,  
1026 12574, <https://doi.org/10.1038/ncomms12574>, 2016a.
- 1027 Li, C., Yan, F., Kang, S., Chen, P., Hu, Z., Gao, S., Qu, B., and Sillanpää, M.: Light absorption  
1028 characteristics of carbonaceous aerosols in two remote stations of the southern fringe of the Tibetan  
1029 Plateau, China, *Atmos. Environ.*, 143, 79-85, <https://doi.org/10.1016/j.atmosenv.2016.08.042>, 2016b.
- 1030 Li, X., Kang, S., Zhang, G., Qu, B., Tripathee, L., Paudyal, R., Jing, Z., Zhang, Y., Yan, F., Li, G., Cui,  
1031 X., Xu, R., Hu, Z., and Li, C.: Light-absorbing impurities in a southern Tibetan Plateau glacier:  
1032 Variations and potential impact on snow albedo and radiative forcing, *Atmos. Res.*, 200, 77-87,  
1033 <https://doi.org/10.1016/j.atmosres.2017.10.002>, 2018.
- 1034 Li, Y. J., Sun, Y., Zhang, Q., Li, X., Li, M., Zhou, Z., and Chan, C. K.: Real-time chemical  
1035 characterization of atmospheric particulate matter in China: A review, *Atmos. Environ.*, 158, 270-304,  
1036 <https://doi.org/10.1016/j.atmosenv.2017.02.027>, 2017.
- 1037 Liu, Y., Sato, Y., Jia, R., Xie, Y., Huang, J., and Nakajima, T.: Modeling study on the transport of summer  
1038 dust and anthropogenic aerosols over the Tibetan Plateau, *Atmos. Chem. Phys.*, 15, 12581-12594,  
1039 <https://doi.org/10.5194/acp-15-12581-2015>, 2015.
- 1040 Liu, Y., Hua, S., Jia, R., and Huang, J.: Effect of Aerosols on the Ice Cloud Properties Over the Tibetan  
1041 Plateau, *J. Geophys. Res. Atmos.*, 124, 9594-9608, <https://doi.org/10.1029/2019jd030463>, 2019.
- 1042 Middlebrook, A. M., Bahreini, R., Jimenez, J. L., and Canagaratna, M. R.: Evaluation of Composition-  
1043 Dependent Collection Efficiencies for the Aerodyne Aerosol Mass Spectrometer using Field Data,  
1044 *Aerosol Sci. Technol.*, 46, 258-271, <https://doi.org/10.1080/02786826.2011.620041>, 2012.
- 1045 Pöhlker, M. L., Pöhlker, C., Ditas, F., Klimach, T., Hrabě de Angelis, I., Araújo, A., Brito, J., Carbone,  
1046 S., Cheng, Y., Chi, X., Ditz, R., Gunthe, S. S., Kesselmeier, J., Könemann, T., Lavrič, J. V., Martin, S.  
1047 T., Mikhailov, E., Moran-Zuloaga, D., Rose, D., Saturno, J., Su, H., Thalman, R., Walter, D., Wang, J.,  
1048 Wolff, S., Barbosa, H. M. J., Artaxo, P., Andreae, M. O., and Pöschl, U.: Long-term observations of  
1049 cloud condensation nuclei in the Amazon rain forest – Part 1: Aerosol size distribution, hygroscopicity,  
1050 and new model parametrizations for CCN prediction, *Atmos. Chem. Phys.*, 16, 15709-15740,  
1051 <https://doi.org/10.5194/acp-16-15709-2016>, 2016.



- 1052 Qiu, J.: The third pole, *Nature*, 454, 393-396, <https://doi.org/10.1038/454393a>, 2008.
- 1053 Ramanathan, V., Ramana, M. V., Roberts, G., Kim, D., Corrigan, C., Chung, C., and Winker, D.: Warming
- 1054 trends in Asia amplified by brown cloud solar absorption, *Nature*, 448, 575-578,
- 1055 <https://doi.org/10.1038/nature06019>, 2007.
- 1056 Ricchiazzi, P., Yang, S., Gautier, C., and Sowle, D.: SBDART: A Research and Teaching Software Tool
- 1057 for Plane-Parallel Radiative Transfer in the Earth's Atmosphere, *Bull. Am. Meteorol. Soc.*, 79, 2101-
- 1058 2114, [https://doi.org/10.1175/1520-0477\(1998\)079<2101:Sarats>2.0.Co;2](https://doi.org/10.1175/1520-0477(1998)079<2101:Sarats>2.0.Co;2), 1998.
- 1059 Rinaldi, M., Gilardoni, S., Paglione, M., Sandrini, S., Fuzzi, S., Massoli, P., Bonasoni, P., Cristofanelli,
- 1060 P., Marinoni, A., Poluzzi, V., and Decesari, S.: Organic aerosol evolution and transport observed at Mt.
- 1061 Cimone (2165 m a.s.l.), Italy, during the PEGASOS campaign, *Atmos. Chem. Phys.*, 15, 11327-11340,
- 1062 <https://doi.org/10.5194/acp-15-11327-2015>, 2015.
- 1063 Rose, D., Nowak, A., Achtert, P., Wiedensohler, A., Hu, M., Shao, M., Zhang, Y., Andreae, M. O., and
- 1064 Poschl, U.: Cloud condensation nuclei in polluted air and biomass burning smoke near the mega-city
- 1065 Guangzhou, China - Part I: Size-resolved measurements and implications for the modeling of aerosol
- 1066 particle hygroscopicity and CCN activity, *Atmos. Chem. Phys.*, 10, 3365-3383,
- 1067 <https://doi.org/10.5194/acp-10-3365-2010>, 2010.
- 1068 Schmale, J., Schneider, J., Nemitz, E., Tang, Y. S., Dragosits, U., Blackall, T. D., Trathan, P. N., Phillips,
- 1069 G. J., Sutton, M., and Braban, C. F.: Sub-Antarctic marine aerosol: dominant contributions from
- 1070 biogenic sources, *Atmos. Chem. Phys.*, 13, 8669-8694, <https://doi.org/10.5194/acp-13-8669-2013>,
- 1071 2013.
- 1072 Schueneman, M. K., Nault, B. A., Campuzano-Jost, P., Jo, D. S., Day, D. A., Schroder, J. C., Palm, B. B.,
- 1073 Hodzic, A., Dibb, J. E., and Jimenez, J. L.: Aerosol pH indicator and organosulfate detectability from
- 1074 aerosol mass spectrometry measurements, *Atmos. Meas. Tech.*, 14, 2237-2260,
- 1075 <https://doi.org/10.5194/amt-14-2237-2021>, 2021.
- 1076 Sun, Y. L., Zhang, Q., Macdonald, A. M., Hayden, K., Li, S. M., Liggio, J., Liu, P. S. K., Anlauf, K. G.,
- 1077 Leaitch, W. R., Steffen, A., Cubison, M., Worsnop, D. R., van Donkelaar, A., and Martin, R. V.: Size-
- 1078 resolved aerosol chemistry on Whistler Mountain, Canada with a high-resolution aerosol mass
- 1079 spectrometer during INTEX-B, *Atmos. Chem. Phys.*, 9, 3095-3111, [https://doi.org/10.5194/acp-9-](https://doi.org/10.5194/acp-9-3095-2009)
- 1080 [3095-2009](https://doi.org/10.5194/acp-9-3095-2009), 2009.
- 1081 Sun, Y. L., Zhang, Q., Schwab, J. J., Demerjian, K. L., Chen, W. N., Bae, M. S., Hung, H. M., Hogrefe,
- 1082 O., Frank, B., Rattigan, O. V., and Lin, Y. C.: Characterization of the sources and processes of organic
- 1083 and inorganic aerosols in New York city with a high-resolution time-of-flight aerosol mass
- 1084 spectrometer, *Atmos. Chem. Phys.*, 11, 1581-1602, <https://doi.org/10.5194/acp-11-1581-2011>, 2011.
- 1085 Takami, A., Miyoshi, T., Shimono, A., and Hatakeyama, S.: Chemical composition of fine aerosol
- 1086 measured by AMS at Fukue Island, Japan during APEX period, *Atmos. Environ.*, 39, 4913-4924,
- 1087 <https://doi.org/10.1016/j.atmosenv.2005.04.038>, 2005.
- 1088 Van Damme, M., Erisman, J. W., Clarisse, L., Dammers, E., Whitburn, S., Clerbaux, C., Dolman, A. J.,
- 1089 and Coheur, P.-F.: Worldwide spatiotemporal atmospheric ammonia (NH<sub>3</sub>) columns variability
- 1090 revealed by satellite, *Geophys. Res. Lett.*, 42, 8660-8668, <https://doi.org/10.1002/2015gl065496>, 2015.
- 1091 Wan, X., Kang, S., Wang, Y., Xin, J., Liu, B., Guo, Y., Wen, T., Zhang, G., and Cong, Z.: Size distribution
- 1092 of carbonaceous aerosols at a high-altitude site on the central Tibetan Plateau (Nam Co Station,
- 1093 4730m.a.s.l.), *Atmos. Res.*, 153, 155-164, <https://doi.org/10.1016/j.atmosres.2014.08.008>, 2015.
- 1094 Wang, J., Ge, X., Chen, Y., Shen, Y., Zhang, Q., Sun, Y., Xu, J., Ge, S., Yu, H., and Chen, M.: Highly
- 1095 time-resolved urban aerosol characteristics during springtime in Yangtze River Delta, China: insights
- 1096 from soot particle aerosol mass spectrometry, *Atmos. Chem. Phys.*, 16, 9109-9127,
- 1097 <https://doi.org/10.5194/acp-16-9109-2016>, 2016.
- 1098 Wang, J., Zhang, Q., Chen, M., Collier, S., Zhou, S., Ge, X., Xu, J., Shi, J., Xie, C., Hu, J., Ge, S., Sun,
- 1099 Y., and Coe, H.: First Chemical Characterization of Refractory Black Carbon Aerosols and Associated
- 1100 Coatings over the Tibetan Plateau (4730 m a.s.l.), *Environ. Sci. Technol.*, 51, 14072-14082,
- 1101 <https://doi.org/10.1021/acs.est.7b03973>, 2017.
- 1102 Xie, C., Xu, W., Wang, J., Wang, Q., Liu, D., Tang, G., Chen, P., Du, W., Zhao, J., Zhang, Y., Zhou, W.,
- 1103 Han, T., Bian, Q., Li, J., Fu, P., Wang, Z., Ge, X., Allan, J., Coe, H., and Sun, Y.: Vertical
- 1104 characterization of aerosol optical properties and brown carbon in winter in urban Beijing, China,
- 1105 *Atmos. Chem. Phys.*, 19, 165-179, <https://doi.org/10.5194/acp-19-165-2019>, 2019.
- 1106 Xu, B., Cao, J., Hansen, J., Yao, T., Joswita, D. R., Wang, N., Wu, G., Wang, M., Zhao, H., Yang, W., Liu,
- 1107 X., and He, J.: Black soot and the survival of Tibetan glaciers, *Proc. Natl. Acad. Sci. USA*, 106, 22114-
- 1108 22118, <https://doi.org/10.1073/pnas.0910444106>, 2009.
- 1109 Xu, J., Wang, Z., Yu, G., Qin, X., Ren, J., and Qin, D.: Characteristics of water soluble ionic species in
- 1110 fine particles from a high altitude site on the northern boundary of Tibetan Plateau: Mixture of mineral
- 1111 dust and anthropogenic aerosol, *Atmos. Res.*, 143, 43-56,





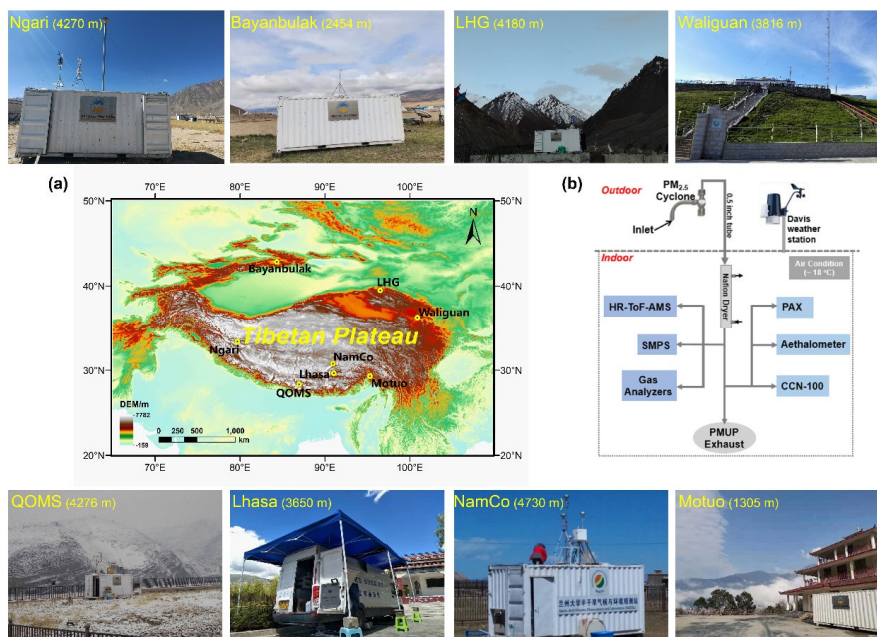
- 1112 <https://doi.org/10.1016/j.atmosres.2014.01.018>, 2014a.
- 1113 Xu, J., Zhang, Q., Chen, M., Ge, X., Ren, J., and Qin, D.: Chemical composition, sources, and processes
- 1114 of urban aerosols during summertime in northwest China: insights from high-resolution aerosol mass
- 1115 spectrometry, *Atmos. Chem. Phys.*, 14, 12593-12611, <https://doi.org/10.5194/acp-14-12593-2014>,
- 1116 2014b.
- 1117 Xu, J., Zhang, Q., Wang, Z. B., Yu, G. M., Ge, X. L., and Qin, X.: Chemical composition and size
- 1118 distribution of summertime PM<sub>2.5</sub> at a high altitude remote location in the northeast of the Qinghai-
- 1119 Xizang (Tibet) Plateau: insights into aerosol sources and processing in free troposphere, *Atmos. Chem.*
- 1120 *Phys.*, 15, 5069-5081, <https://doi.org/10.5194/acp-15-5069-2015>, 2015.
- 1121 Xu, J., Shi, J., Zhang, Q., Ge, X., Canonaco, F., Prévôt, A. S. H., Vonwiller, M., Szidat, S., Ge, J., Ma, J.,
- 1122 An, Y., Kang, S., and Qin, D.: Wintertime organic and inorganic aerosols in Lanzhou, China: sources,
- 1123 processes, and comparison with the results during summer, *Atmos. Chem. Phys.*, 16, 14937-14957,
- 1124 <https://doi.org/10.5194/acp-16-14937-2016>, 2016.
- 1125 Xu, J., Zhang, Q., Shi, J., Ge, X., Xie, C., Wang, J., Kang, S., Zhang, R., and Wang, Y.: Chemical
- 1126 characteristics of submicron particles at the central Tibetan Plateau: insights from aerosol mass
- 1127 spectrometry, *Atmos. Chem. Phys.*, 18, 427-443, <https://doi.org/10.5194/acp-18-427-2018>, 2018.
- 1128 Xu, J., Hettiyadura, A. P. S., Liu, Y., Zhang, X., Kang, S., and Laskin, A.: Regional Differences of
- 1129 Chemical Composition and Optical Properties of Aerosols in the Tibetan Plateau, *J. Geophys. Res.*
- 1130 *Atmos.*, 125, <https://doi.org/10.1029/2019jd031226>, 2020.
- 1131 Xu, J.: High-time-resolution dataset of atmospheric aerosols over the Tibetan Plateau and its
- 1132 surroundings (2015-2021), National Cryosphere Desert Data Center [Data set],
- 1133 <https://doi.org/10.12072/ncdc.NIEER.db2200.2022>, 2022.
- 1134 Xu, J., Hettiyadura, A. P. S., Liu, Y., Zhang, X., Kang, S., and Laskin, A.: Atmospheric Brown Carbon
- 1135 on the Tibetan Plateau: Regional Differences in Chemical Composition and Light Absorption
- 1136 Properties, *Environmental Science & Technology Letters*, 9, 219-225,
- 1137 <https://doi.org/10.1021/acs.estlett.2c00016>, 2022.
- 1138 Yao, T., Thompson, L., Mosbrugger, V., Zhang, F., Ma, Y., Luo, T., Xu, B., Yang, X., Joswiak, D. R.,
- 1139 Wang, W., Joswiak, M. E., Devkota, L. P., Tayal, S., Jilani, R., and Fayziev, R.: Third Pole Environment
- 1140 (TPE), *Environ. Dev.*, 3, 52-64, <https://doi.org/10.1016/j.envdev.2012.04.002>, 2012.
- 1141 Yao, T., Xue, Y., Chen, D., Chen, F., Thompson, L., Cui, P., Koike, T., Lau, W. K. M., Lettenmaier, D.,
- 1142 Mosbrugger, V., Zhang, R., Xu, B., Dozier, J., Gillespie, T., Gu, Y., Kang, S., Piao, S., Sugimoto, S.,
- 1143 Ueno, K., Wang, L., Wang, W., Zhang, F., Sheng, Y., Guo, W., Ailikun, Yang, X., Ma, Y., Shen, S. S.
- 1144 P., Su, Z., Chen, F., Liang, S., Liu, Y., Singh, V. P., Yang, K., Yang, D., Zhao, X., Qian, Y., Zhang, Y.,
- 1145 and Li, Q.: Recent Third Pole's Rapid Warming Accompanies Cryospheric Melt and Water Cycle
- 1146 Intensification and Interactions between Monsoon and Environment: Multidisciplinary Approach with
- 1147 Observations, Modeling, and Analysis, *Bull. Am. Meteorol. Soc.*, 100, 423-444,
- 1148 <https://doi.org/10.1175/bams-d-17-0057.1>, 2019.
- 1149 You, Q., Cai, Z., Pepin, N., Chen, D., Ahrens, B., Jiang, Z., Wu, F., Kang, S., Zhang, R., Wu, T., Wang,
- 1150 P., Li, M., Zuo, Z., Gao, Y., Zhai, P., and Zhang, Y.: Warming amplification over the Arctic Pole and
- 1151 Third Pole: Trends, mechanisms and consequences, *Earth-Science Reviews*, 217, 103625,
- 1152 <https://doi.org/10.1016/j.earscirev.2021.103625>, 2021.
- 1153 Zhang, N., Cao, J., Liu, S., Zhao, Z., Xu, H., and Xiao, S.: Chemical composition and sources of PM<sub>2.5</sub>
- 1154 and TSP collected at Qinghai Lake during summertime, *Atmos. Res.*, 138, 213-222,
- 1155 <https://doi.org/10.1016/j.atmosres.2013.11.016>, 2014.
- 1156 Zhang, Q., Alfarra, M. R., Worsnop, D. R., Allan, J. D., Coe, H., Canagaratna, M. R., and Jimenez, J. L.:
- 1157 Deconvolution and quantification of hydrocarbon-like and oxygenated organic aerosols based on
- 1158 aerosol mass spectrometry, *Environ. Sci. Technol.*, 39, 4938-4952, <https://doi.org/10.1021/es048568l>,
- 1159 2005a.
- 1160 Zhang, Q., Canagaratna, M. R., Jayne, J. T., Worsnop, D. R., and Jimenez, J. L.: Time- and size-resolved
- 1161 chemical composition of submicron particles in Pittsburgh: Implications for aerosol sources and
- 1162 processes, *J. Geophys. Res. Atmos.*, 110, D07S09, <https://doi.org/10.1029/2004jd004649>, 2005b.
- 1163 Zhang, Q., Jimenez, J. L., Canagaratna, M. R., Allan, J. D., Coe, H., Ulbrich, I., Alfarra, M. R., Takami,
- 1164 A., Middlebrook, A. M., Sun, Y. L., Dzepina, K., Dunlea, E., Docherty, K., DeCarlo, P. F., Salcedo, D.,
- 1165 Onasch, T., Jayne, J. T., Miyoshi, T., Shimojo, A., Hatakeyama, S., Takegawa, N., Kondo, Y.,
- 1166 Schneider, J., Drewnick, F., Borrmann, S., Weimer, S., Demerjian, K., Williams, P., Bower, K.,
- 1167 Bahreini, R., Cottrell, L., Griffin, R. J., Rautiainen, J., Sun, J. Y., Zhang, Y. M., and Worsnop, D. R.:
- 1168 Ubiquity and dominance of oxygenated species in organic aerosols in anthropogenically-influenced
- 1169 Northern Hemisphere midlatitudes, *Geophys. Res. Lett.*, 34, L13801,
- 1170 <https://doi.org/10.1029/2007gl029979>, 2007a.
- 1171 Zhang, Q., Jimenez, J. L., Worsnop, D., and Canagaratna, M.: A case study of urban particle acidity and



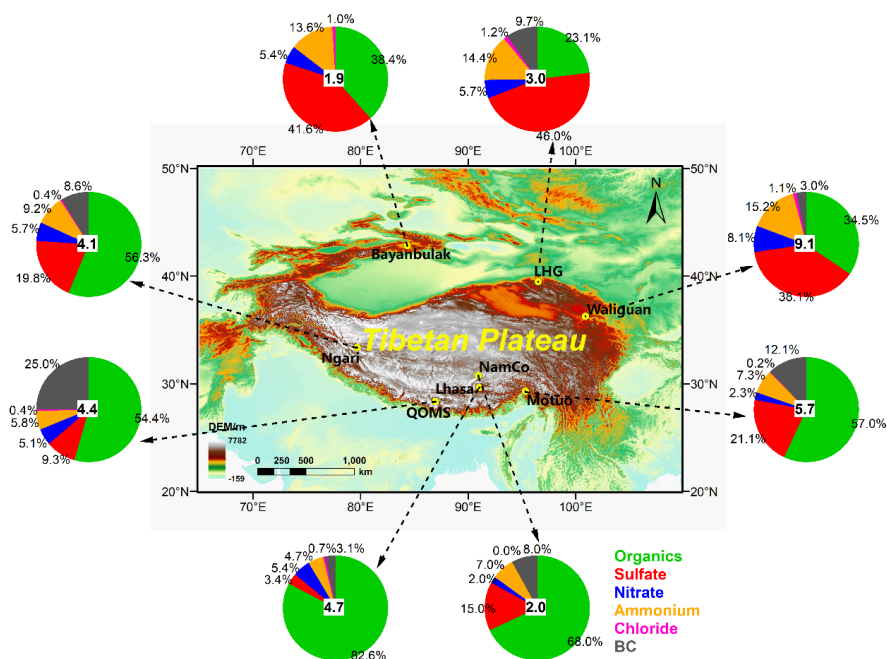
1172 its influence on secondary organic aerosol, *Environ. Sci. Technol.*, 41, 3213-3219,  
1173 <https://doi.org/10.1021/es061812j>, 2007b.  
1174 Zhang, X., Xu, J., Kang, S., Liu, Y., and Zhang, Q.: Chemical characterization of long-range transport  
1175 biomass burning emissions to the Himalayas: insights from high-resolution aerosol mass spectrometry,  
1176 *Atmos. Chem. Phys.*, 18, 4617–4638, <https://doi.org/10.5194/acp-18-4617-2018>, 2018.  
1177 Zhang, X., Xu, J., Kang, S., Zhang, Q., and Sun, J.: Chemical characterization and sources of submicron  
1178 aerosols in the northeastern Qinghai–Tibet Plateau: insights from high-resolution mass spectrometry,  
1179 *Atmos. Chem. Phys.*, 19, 7897–7911, <https://doi.org/10.5194/acp-19-7897-2019>, 2019.  
1180 Zhang, X., Xu, J., and Kang, S.: Chemical characterization of submicron particulate matter (PM<sub>1</sub>) emitted  
1181 by burning highland barley in the northeastern part of the Qinghai–Tibet Plateau, *Atmos. Environ.*,  
1182 224, 117351, <https://doi.org/10.1016/j.atmosenv.2020.117351>, 2020.  
1183 Zhang, X., Xu, J., Kang, S., Sun, J., Shi, J., Gong, C., Sun, X., Du, H., Ge, X., and Zhang, Q.: Regional  
1184 Differences in the Light Absorption Properties of Fine Particulate Matter Over the Tibetan Plateau:  
1185 Insights From HR-ToF-AMS and Aethalometer Measurements, *J. Geophys. Res. Atmos.*, 126,  
1186 <https://doi.org/10.1029/2021jd035562>, 2021.  
1187 Zhao, W., Zhang, X., Zhai, L., Shen, X., and Xu, J.: Chemical characterization and sources of submicron  
1188 aerosols in Lhasa on the Qinghai–Tibet Plateau: Insights from high-resolution mass spectrometry, *Sci.*  
1189 *Total Environ.*, 815, <https://doi.org/10.1016/j.scitotenv.2021.152866>, 2022.  
1190 Zhao, Z., Cao, J., Shen, Z., Xu, B., Zhu, C., Chen, L.-W. A., Su, X., Liu, S., Han, Y., Wang, G., and Ho,  
1191 K.: Aerosol particles at a high-altitude site on the Southeast Tibetan Plateau, China: Implications for  
1192 pollution transport from South Asia, *J. Geophys. Res. Atmos.*, 118, 11360-11375,  
1193 <https://doi.org/10.1002/jgrd.50599>, 2013.  
1194 Zheng, J., Hu, M., Du, Z., Shang, D., Gong, Z., Qin, Y., Fang, J., Gu, F., Li, M., Peng, J., Li, J., Zhang,  
1195 Y., Huang, X., He, L., Wu, Y., and Guo, S.: Influence of biomass burning from South Asia at a high-  
1196 altitude mountain receptor site in China, *Atmos. Chem. Phys.*, 17, 6853-6864,  
1197 <https://doi.org/10.5194/acp-17-6853-2017>, 2017.  
1198 Zhou, S., Collier, S., Jaffe, D. A., Briggs, N. L., Hee, J., Sedlacek Iii, A. J., Kleinman, L., Onasch, T. B.,  
1199 and Zhang, Q.: Regional influence of wildfires on aerosol chemistry in the western US and insights  
1200 into atmospheric aging of biomass burning organic aerosol, *Atmos. Chem. Phys.*, 17, 2477-2493,  
1201 <https://doi.org/10.5194/acp-17-2477-2017>, 2017.  
1202 Zhou, T., and Zhang, W.: Anthropogenic warming of Tibetan Plateau and constrained future projection,  
1203 *Environ. Res. Lett.*, 16, 044039, <https://doi.org/10.1088/1748-9326/abede8>, 2021.  
1204 Zhou, W., Xu, W., Kim, H., Zhang, Q., Fu, P., Worsnop, D. R., and Sun, Y.: A review of aerosol chemistry  
1205 in Asia: insights from aerosol mass spectrometer measurements, *Environ. Sci.: Proc. Imp.*,  
1206 <https://doi.org/10.1039/D0EM00212G>, 2020.  
1207 Zhu, C.-S., Cao, J.-J., Ho, K.-F., Antony Chen, L. W., Huang, R.-J., Wang, Y.-C., Li, H., Shen, Z.-X.,  
1208 Chow, J. C., Watson, J. G., Su, X.-L., Wang, Q.-y., and Xiao, S.: The optical properties of urban aerosol  
1209 in northern China: A case study at Xi'an, *Atmos. Res.*, 160, 59-67,  
1210 <https://doi.org/10.1016/j.atmosres.2015.03.008>, 2015.  
1211 Zhu, Q., He, L. Y., Huang, X. F., Cao, L. M., Gong, Z. H., Wang, C., Zhuang, X., and Hu, M.:  
1212 Atmospheric aerosol compositions and sources at two national background sites in northern and  
1213 southern China, *Atmos. Chem. Phys.*, 16, 10283-10297, <https://doi.org/10.5194/acp-16-10283-2016>,  
1214 2016.  
1215



1216 **Figures**

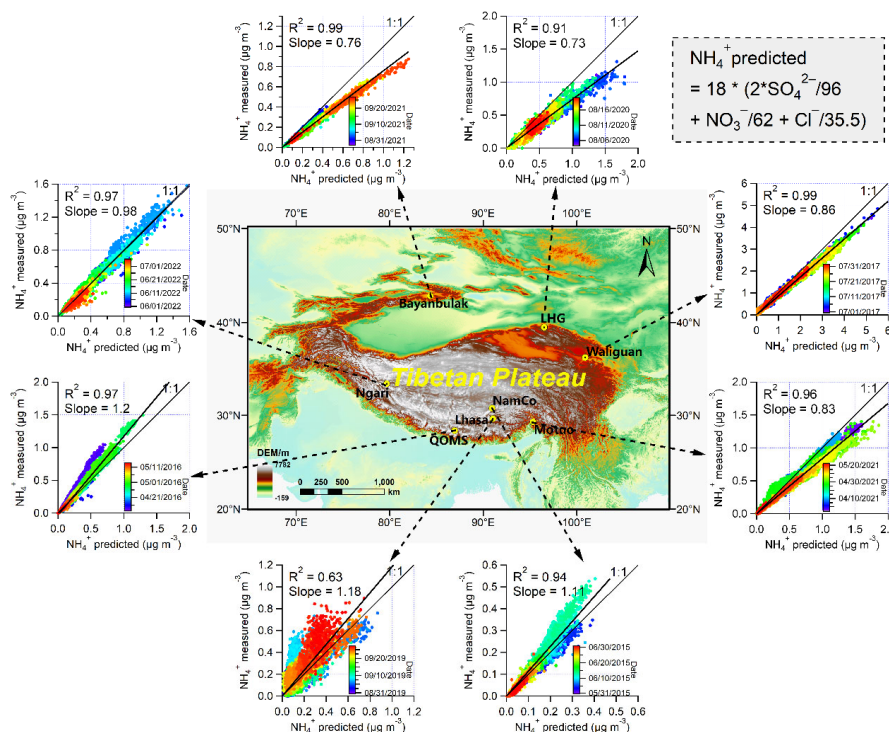


1217  
1218 **Figure 1.** (a) Geographical locations of the observation sites (see Table 1 for full name and  
1219 characteristics of each site) in the Tibetan Plateau and its surroundings in this study (The  
1220 geographical base map is created with ArcGIS). Fieldwork photographs illustrate the real  
1221 observation conditions and surroundings at each site. (b) The normal sampling setups of instruments  
1222 during the online aerosol observations.



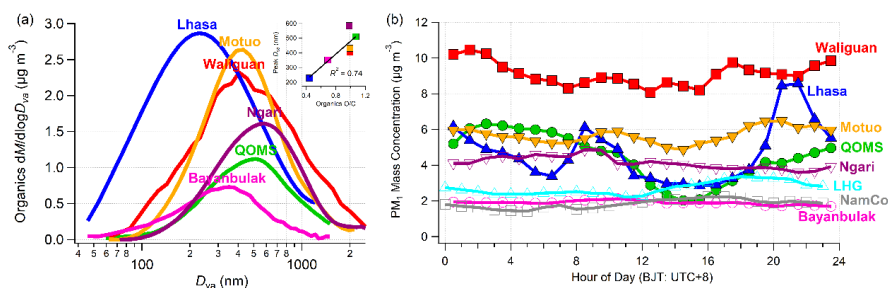
1223

1224 **Figure 2.** Regional distribution of average mass concentrations (values marked in the central of  
 1225 each pie chart with unit of  $\mu\text{g m}^{-3}$ ) and chemical compositions (percentage values around each pie  
 1226 chart) of submicron aerosols ( $\text{PM}_{10}$ ) during the eight online aerosol field measurements in the Tibetan  
 1227 Plateau and its surroundings (The geographical base map is created with ArcGIS).



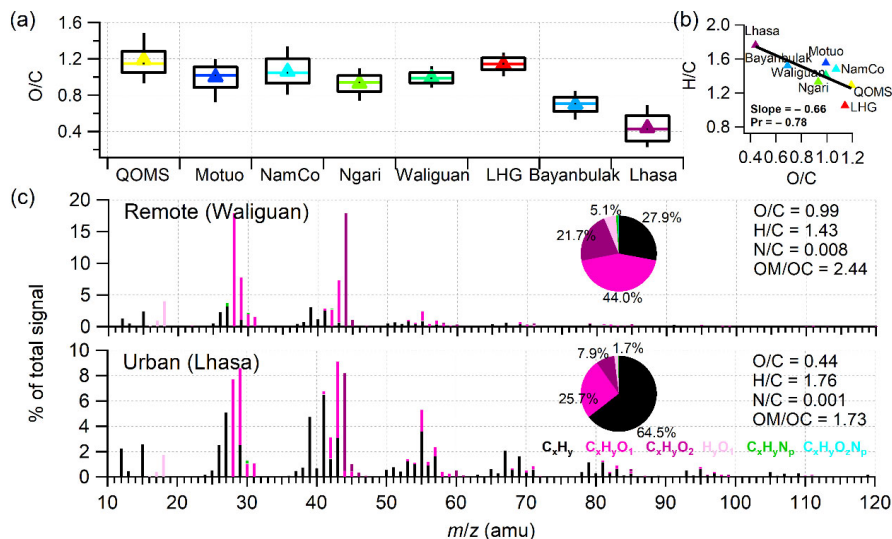
1228

1229 **Figure 3.** Regional difference of bulk acidity of submicron aerosols based on the scatterplot analysis  
1230 and linear regression of measured  $NH_4^+$  versus predicted  $NH_4^+$  during the eight aerosol field  
1231 measurement campaigns in the Tibetan Plateau and its surroundings (The geographical base map is  
1232 created with ArcGIS).



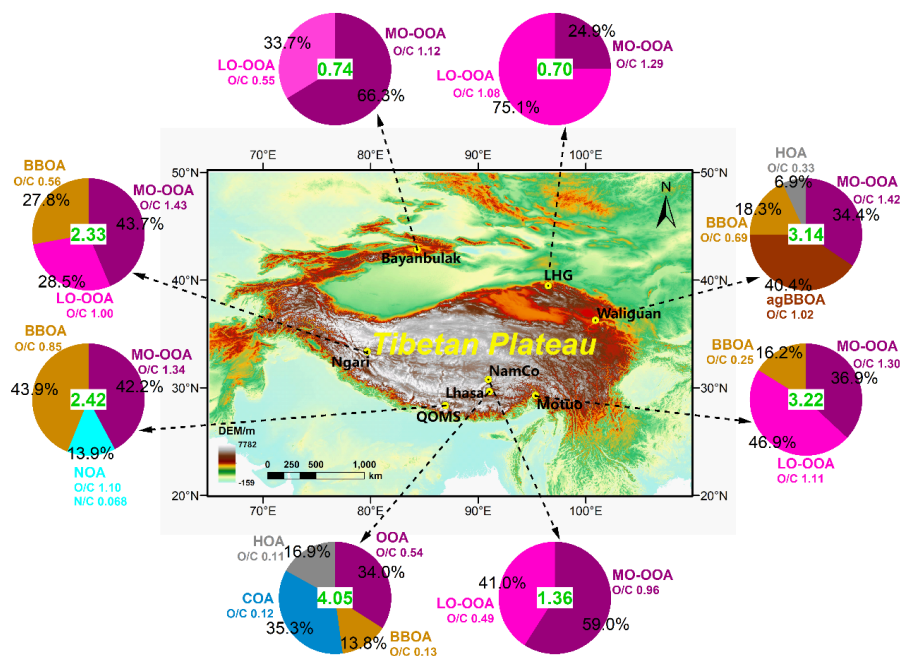
1233

1234 **Figure 4.** (a) Average size distributions of organic mass concentrations during six field  
 1235 measurement campaigns in the Tibetan Plateau and its surroundings. (b) Diurnal variations of total  
 1236 PM<sub>1</sub> mass concentrations during the eight field measurement campaigns in the Tibetan Plateau and  
 1237 its surroundings. Insert graph in (a) is the scatter plot of peak diameters in these size distributions  
 1238 versus the average O/C ratio of organics.



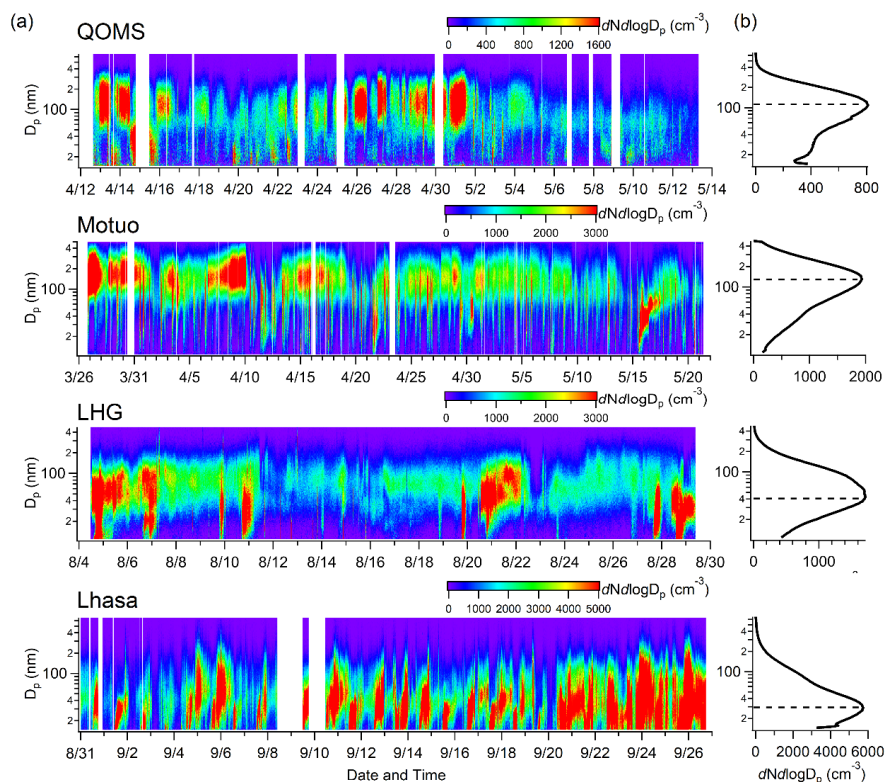
1239

1240 **Figure 5.** (a) Box plots of the average O/C ratios and (b) Van Krevelen diagram of H/C versus O/C  
 1241 among the eight field measurement campaigns in this study. (c) The average HRMSs of OA colored  
 1242 with different ion categories during the Waliguan and Lhasa measurement campaigns. The whiskers  
 1243 of boxes indicate the 90<sup>th</sup> and 10<sup>th</sup> percentiles, the upper and lower boundaries of boxes indicate the  
 1244 75<sup>th</sup> and 25<sup>th</sup> percentiles, the lines in the boxes indicate the median values, the markers indicate the  
 1245 mean values, and similarly hereinafter.



1246

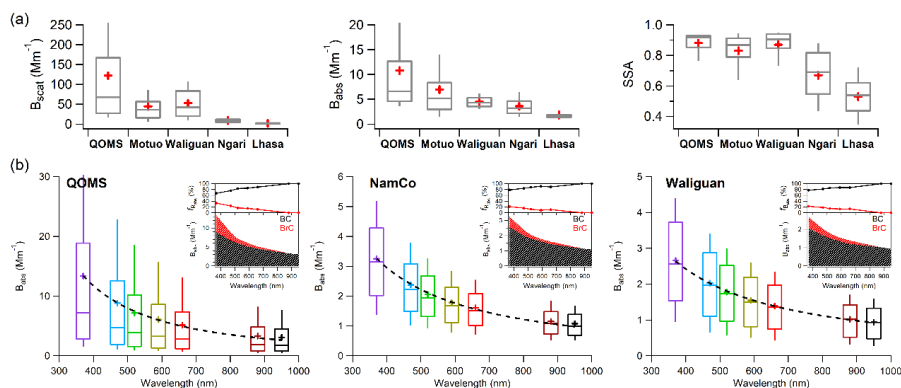
1247 **Figure 6.** Regional distribution of OA components from PMF source apportionment during the eight  
 1248 online aerosol field measurements in the Tibetan Plateau and its surroundings (The geographical  
 1249 base map is created with ArcGIS). Values marked in the central of each pie chart are average OA  
 1250 mass with unit of  $\mu\text{g m}^{-3}$  while the percentage values around the pie chart are the mass contributions  
 1251 of each OA component. The O/C ratio of each OA component is also marked around each pie chart.



1252

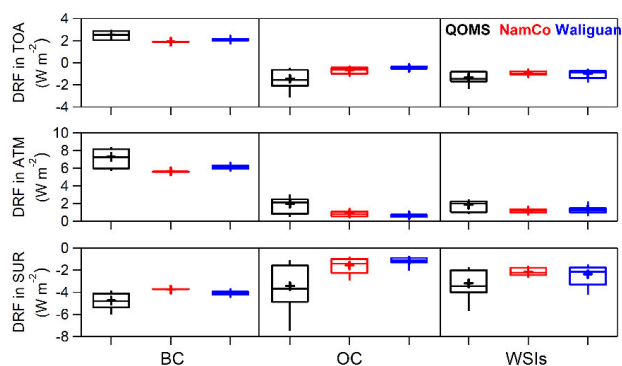
1253 **Figure 7. (a)** Temporal variations of the size distributions of particle number concentrations during  
1254 the aerosol field measurement campaigns at QOMS, Motuo, LHG, and Lhasa sites. **(b)** The average  
1255 size distribution of particle number concentration during entire measurement period at each site.





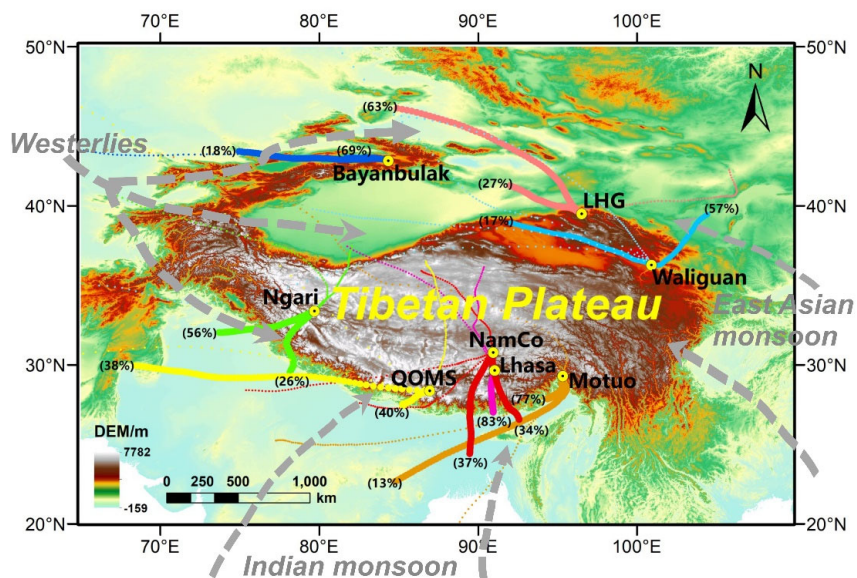
1256

1257 **Figure 8.** Box plots of (a) the average particle light scattering coefficient ( $B_{scat}$ ), light absorption  
 1258 coefficient ( $B_{abs}$ ), and single scattering albedo (SSA) during the five aerosol field measurement  
 1259 campaigns at QOMS, Motuo, Waliguan, Ngari, and Lhasa sites, and (b) the particle  $B_{abs}$  at seven  
 1260 wavelengths measured by aethalometers at QOMS, NamCo, and Waliguan sites. The dashed lines  
 1261 in the boxes in (b) show the power-law fit of the average  $B_{abs}$  as a function of wavelength. The  
 1262 inserted plots in (b) are the apportioned contributions of BC and BrC to total  $B_{abs}$  at different  
 1263 wavelengths.



1264

1265 **Figure 9.** Box-plots of the modelled direct radiative forcing (DRF) at the top of the atmosphere  
 1266 (TOA), the atmosphere (ATM), and the earth's surface (SUR) caused by black carbon (BC), organic  
 1267 carbon (OC), and water-soluble ions (WSIs) during the QOMS, NamCo, and Waliguan campaigns.



1268

1269 **Figure 10.** The average air mass backward trajectory clusters during the eight field campaigns in  
1270 the Tibetan Plateau and its surroundings in our study (The geographical base map is created with  
1271 ArcGIS). The major trajectory clusters belong to each field campaign are displayed using the  
1272 relatively large solid circles in different colors with contributions marked in the corresponding  
1273 brackets, while the rest clusters with less contributions are exhibited in small dots.



1274 **Tables**

1275 **Table 1.** Detailed information about the full name and geographic characteristic of observation  
 1276 station, sample period, online instruments, and corresponding references during each aerosol field  
 1277 measurement campaigns over the Tibetan Plateau and its surroundings in this study.

Station	Full Station Name	Lat. (°N)	Long. (°E)	Alt. (m)	Sample Period	Online Instruments					References	
						HR-ToF-AMS		SMPS	PAX	Aethal ometer		CCN -100
						MS	PToF					
QOMS	Qomolangma Station for Atmospheric and Environmental Observation and Research, Chinese Academy of Sciences	28.36	86.95	4276	12 April to 12 May 2016	✓	✓	✓	✓	✓	Zhang et al. (2018) An et al. (2019) Xu et al. (2020) Zhang et al. (2021) Xu et al. (2022)	
Motuo	Motuo County, Linzhi City, Tibet Autonomous Region, China	29.30	95.32	1305	26 Mar to 22 May 2021	✓	✓	✓	✓		This study	
NamCo	Nam Co Station for Multisphere Observation and Research, Chinese Academy of Sciences	30.77	90.95	4730	31 May to 1 July 2015	✓			✓		Xu et al. (2018) Zhang et al. (2021)	
Ngari	Ngari Station for Desert Environment Observation and Research, Chinese Academy of Sciences	33.39	79.70	4270	1 Jun to 5 Jul 2022	✓	✓		✓		This study	
Waliguan	China Global Atmospheric Watch Baseline Observatory, Mount Waliguan Base	36.28	100.90	3816	1 July to 31 July 2017	✓	✓		✓	✓	Zhang et al. (2019) Zhang et al. (2020) Xu et al. (2020) Zhang et al. (2021) Xu et al. (2022)	
LHG	Qilian Observation and Research Station of Cryosphere and Ecologic Environment, Chinese Academy of Sciences	39.50	96.51	4180	4 August to 29 August 2020	✓		✓		✓	This study	
Bayanbulak	Bayanbulak Town, Hejing County, Bayingolin Mongolian Autonomous Prefecture, Xinjiang Uygur Autonomous Region, China	42.83	84.35	2454	29 August to 26 September 2021	✓	✓				This study	
Lhasa	Lhasa City, Tibet Autonomous Region, China	29.65	91.03	3650	31 August to 26 September 2019	✓	✓	✓	✓		Zhao et al. (2022)	

1278



1279 **Table 2.** Summary of the average values measured with various instruments during the eight aerosol  
 1280 field measurement campaigns in the TP and its surroundings in this study.

Measurement items	QOMS	Motuo	NamCo	Ngari	Waliguan	LHG	Bayanbulak	Lhasa
<b>HR-ToF-AMS measurements</b>								
PM <sub>1</sub> mass conc. ( $\mu\text{g m}^{-3}$ )	4.4	5.7	2.0	4.1	9.1	3.0	1.9 <sup>a</sup>	4.7
PM <sub>1</sub> chemical compositions (%)								
OA	54.4	57.0	68.0	56.3	34.5	23.1	38.4	82.6
Sulfate	9.3	21.1	15.0	19.8	38.1	46.0	41.6	3.4
Nitrate	5.1	2.3	2.0	5.7	8.1	5.7	5.4	5.4
Ammonium	5.8	7.3	7.0	9.2	15.2	14.4	13.6	4.7
Chloride	0.4	0.2	0	0.4	1.1	1.2	1.0	0.7
BC	25.0	12.1	8.0	8.6	3.0	9.7	N/A	3.1
Peak diameter in mass size distribution (nm)								
OA	510.2	430.5		584.4	405.5		350.8	228.1
SNA	510.2	471.9		634.5	504.7		379.6	250.0
OA components (%)								
MO-OOA	42.2	36.9	59.0	43.7	34.4	24.9	66.3	
LO-OOA		46.9	41.0	28.5		75.1	33.7	
OOA								34.0
BBOA	3.9	16.2		27.8	18.3			13.8
agBBOA					40.4			
NOA	13.9							
HOA					6.9			16.9
COA								35.3
OA elemental ratios								
O/C	1.19	0.99	1.07	0.98	0.99	1.14	0.69	0.44
H/C	1.29	1.55	1.48	1.33	1.41	1.05	1.52	1.76
OM/OC	2.70	2.48	2.57	2.44	2.45	2.62	2.09	1.74
N/C	0.030	0.020	0.016	0.019	0.008	0.011	0.026	0.001
<b>SMPS measurements</b>								
Number conc. ( $\text{cm}^{-3}$ )	709.3	1639.2				1462.0		3994.4
Peak diameter in PNSD (nm)	109.4	131.0				42.9		28.9
<b>PAX measurements</b>								
$B_{\text{scat}}$ ( $\text{Mm}^{-1}$ )	121.9	44.9		8.9	36.3			2.1
$B_{\text{abs}}$ ( $\text{Mm}^{-1}$ )	10.8	7.0		3.6	4.1			1.9
$B_{\text{ext}}$ ( $\text{Mm}^{-1}$ )	132.7	51.9		12.6	40.4			4.0
SSA	0.89	0.83		0.67	0.86			0.52
<b>Aethalometer measurements</b>								
$B_{\text{abs},370}$ ( $\text{Mm}^{-1}$ )	13.40		3.25		2.66			
Absorption Ångström exponent	1.73		1.28		1.12			
$B_{\text{abs},\text{BrC},370}$ ( $\text{Mm}^{-1}$ )	4.42		0.69		0.60			
$B_{\text{abs},\text{BC},370}$ ( $\text{Mm}^{-1}$ )	8.94		2.56		2.06			
$f_{B_{\text{abs},\text{BrC},370}}$ (%)	33.1		21.3		22.4			
$f_{B_{\text{abs},\text{BC},370}}$ (%)	66.9		78.7		77.6			
<b>CCN-100 measurements (<math>\text{cm}^{-3}</math>)</b>								
CCN number conc. (SS 0.2%)		974.0			507.0	83.9		
CCN number conc. (SS 0.4%)		1142.6			805.1	344.3		
CCN number conc. (SS 0.6%)		1240.1			1073.3	429.9		
CCN number conc. (SS 0.8%)		1296.5			1230.6	480.8		
CCN number conc. (SS 1.0%)		1337.9			1336.6	516.1		

1281 <sup>a</sup>only non-refractory PM<sub>1</sub> is reported at Bayanbulak due to the absence of BC observation.



1282 **Table 3.** Summary of the average PM<sub>1</sub> mass concentrations ( $\mu\text{g m}^{-3}$ ) measured by the Aerodyne  
 1283 AMSs at various high-altitude and remote sites worldwide.

Observation Sites	Latitude (°N)	Longitude (°E)	Altitude (m a.s.l.)	PM <sub>1</sub> mass ( $\mu\text{g m}^{-3}$ )	References
QOMS, China	28.36	86.95	4276	4.4	This study & Zhang et al. (2018)
Motuo, China	29.30	95.32	1305	5.7	This study
NamCo, China	30.77	90.95	4730	2.0	This study & Xu et al. (2018)
Ngari, China	33.39	79.70	4270	4.1	This study
Waliguan, China	36.28	100.90	3816	9.1	This study & Zhang et al. (2019)
LHG, China	39.50	96.51	4180	3.0	This study
Bayanbulak, China	42.83	84.35	2454	1.9 <sup>a</sup>	This study
Lhasa, China	29.65	91.03	3650	4.7	This study & Zhao et al. (2022)
NamCo, China	30.77	90.95	4730	1.06	Wang et al. (2017)
Mt. Yulong, China	27.20	100.20	3410	5.7	Zheng et al. (2017)
Menyuan, China	37.61	101.26	3295	11.4	Du et al. (2015)
Mt. Wuzhi, China	18.84	109.49	958	10.9	Zhu et al. (2016)
Mt. Jungfrauoch, Switzerland	46.55	7.98	3580	0.55	Fröhlich et al. (2015)
Mt. Jungfrauoch, Switzerland	46.55	7.98	3580	2.24	Zhang et al. (2007a)
Mt. Bachelor, USA	43.98	-121.69	2800	15.10	Zhou et al. (2017)
Mt. Whistler, Canada	50.01	-122.95	2182	1.91	Sun et al. (2009)
Mt. Cimone, Italy	44.18	10.70	2165	4.5	Rinaldi et al. (2015)
Puy de Dôme, France	45.77	2.95	1465	5.58	Freney et al. (2011)
Sub-Antarctic Bird Island	-54.00	-38.04		0.46	Schmale et al. (2013)
Mace Head, Ireland	53.30	-9.80		1.53	Zhang et al. (2007a)
Hyytiälä, Finland	61.90	24.30		2.04	Zhang et al. (2007a)
Storm Peak, USA	40.50	-106.70		2.11	Zhang et al. (2007a)
Duke Forest, USA	36.00	-79.10		2.82	Zhang et al. (2007a)
Chebogue, Canada	43.80	-66.10		2.91	Zhang et al. (2007a)
Okinawa Island, Japan	26.87	33.51		7.89	Jimenez et al. (2009)
Fukue Island, Japan	32.69	128.84		12.03	Takami et al. (2005)
Cheju Island, Korea	33.51	126.50		10.66	Jimenez et al. (2009)

1284 <sup>a</sup>only non-refractory PM<sub>1</sub> is reported at Bayanbulak due to the absence of BC observation.